



Morphological Types of DM Halos in Milky Way-like Galaxies in the TNG50 Simulation: Simple, Twisted, or Stretched

Razieh Emami¹, Shy Genel^{2,3}, Lars Hernquist¹, Charles Alcock¹, Sownak Bose¹, Rainer Weinberger¹, Mark Vogelsberger⁴, Federico Marinacci⁵, Abraham Loeb¹, Paul Torrey⁶, and John C. Forbes²

¹ Center for Astrophysics | Harvard & Smithsonian, 60 Garden Street, Cambridge, MA 02138, USA; razieh.emami_meibody@cfa.harvard.edu

² Center for Computational Astrophysics, Flatiron Institute, New York, NY 10010, USA

³ Columbia Astrophysics Laboratory, Columbia University, 550 West 120th Street, New York, NY 10027, USA

⁴ Department of Physics, Kavli Institute for Astrophysics and Space Research, Massachusetts Institute of Technology, Cambridge, MA 02139, USA

⁵ Department of Physics & Astronomy “Augusto Righi”, University of Bologna, via Gobetti 93/2, I-40129 Bologna, Italy

⁶ Department of Astronomy, University of Florida, 211 Bryant Space Sciences Center, Gainesville, FL 32611, USA

Received 2020 September 24; revised 2021 January 21; accepted 2021 March 22; published 2021 May 21

Abstract

We present a comprehensive analysis of the shape of dark matter (DM) halos in a sample of 25 Milky Way-like galaxies in TNG50 simulation. Using an enclosed volume iterative method, we infer an oblate-to-triaxial shape for the DM halo with median $T \simeq 0.24$. We group DM halos into three different categories. Simple halos (32% of the population) establish principal axes whose ordering in magnitude does not change with radius and whose orientations are almost fixed throughout the halo. Twisted halos (32%) experience levels of gradual rotations throughout their radial profiles. Finally, stretched halos (36%) demonstrate a stretching in the lengths of their principal axes where the ordering of different eigenvalues changes with radius. Subsequently, the halo experiences a “rotation” of $\sim 90^\circ$ where the stretching occurs. Visualizing the 3D ellipsoid of each halo, for the first time, we report signs of a reorienting ellipsoid in twisted and stretched halos. We examine the impact of baryonic physics on DM halo shape through a comparison to dark matter only (DMO) simulations. This suggests a triaxial (prolate) halo. We analyze the impacts of substructure on DM halo shape in both hydrodynamical and DMO simulations and confirm that they are subdominant. We study the distribution of satellites in our sample. In simple and twisted halos, the angle between satellites’ angular momentum and the galaxy’s angular momentum grows with radius. However, stretched halos show a flat distribution of angles. Overlaying our theoretical outcome on the observational results presented in the literature establishes a fair agreement.

Unified Astronomy Thesaurus concepts: Milky Way Galaxy (1054); Galaxy classification systems (582); Cold dark matter (265); Hydrodynamical simulations (767)

1. Introduction

The morphologies of galaxies are affected by a number of dynamical mechanisms operating throughout the history of galaxy evolution. Star formation, accretion of gas, galaxy mergers, and feedback from supermassive black holes (SMBHs) play important roles in shaping galaxies. Structural morphology of galaxies, in general, can be assessed from the analysis of their three-dimensional shape. As the 3D shape of a galaxy describes the spatial distribution of mass, it provides an exceptional description of galaxy morphology.

Observationally, several studies have measured the shape of the dark matter (DM) halo of the Milky Way (MW) galaxy; to do so, different tracers have been used, such as the orbit of the Sgr dwarf (Ibata et al. 2001; Johnston et al. 2005), the radial velocities (Johnston et al. 2005) or the line-of-sight velocities (Helmi 2004) of M-giant candidates for modeling Sgr dwarf debris, kinematics of K dwarfs (Garbari et al. 2012), the tidal stream from Palomar5 (Pal5) (Küpper et al. 2015), or the proper motion of globular clusters (Posti & Helmi 2019). As pointed out below, each of these techniques gives rise to slightly different results. It is therefore beneficial to use high-resolution cosmological simulations, which cover all of the aforementioned effects, to estimate the shape of halos and compare them with different observational results.

There have been significant developments in the study of galaxy morphology using high-resolution hydrodynamical simulations such as AURIGA (Monachesi et al. 2016;

Grand et al. 2018; Hani et al. 2019), EAGLE (Crain et al. 2015; Schaye et al. 2015; Trayford et al. 2019; Font et al. 2020; Santistevan et al. 2020), FIRE (Garrison-Kimmel et al. 2018; El-Badry et al. 2018; Orr et al. 2020; Sanderson et al. 2020), and NIHAO-UHD (Buck et al. 2018, 2020). In addition, there have been a number of such studies using the Illustris simulation (Vogelsberger et al. 2014a, 2014b; Genel et al. 2014; Sijacki et al. 2015) as well as the IllustrisTNG simulations (Naiman et al. 2018; Nelson et al. 2018; Marinacci et al. 2018; Pillepich et al. 2018; Springel et al. 2018; Vogelsberger et al. 2020; Merritt et al. 2020). Thanks to these modern simulations, we can produce realistic galaxy populations with reliable data suitable for our theoretical investigations. The shapes of elliptical and spiral galaxies are well described with triaxial ellipsoids (Sandage et al. 1970; Lambas et al. 1992) with three different axis lengths ($a \leq b \leq c$). From these axis lengths we can read three broad geometrical types: oblate (disky) galaxies have $c \simeq b > a$, prolate (elongated) galaxies are associated with $c > b \simeq a$, and spheroidal galaxies correspond to $a \simeq b \simeq c$. Conventionally, the shape of galaxies is described by the following parameters: the minor-to-major axis ratio, $s \equiv a/c$, as well as the intermediate-to-major axis ratio, $q \equiv b/c$. In addition, using the above shape parameters, one can infer the triaxiality parameter as $T \equiv (1 - q^2)/(1 - s^2)$, to categorize the galaxy shapes. Here $T = 0$ (1) refers to a perfect oblate (prolate) spheroid. Conventionally, Schneider et al. (2012) defines $T \leq 0.33$ to indicate an oblate ellipsoid,

Table 1
Physical Parameters of the TNG50 Simulation

Name	Volume (Mpc ³)	L_{box} (Mpc h^{-1})	N_{Gas}	N_{DM}	m_{baryon} ($10^5 M_{\odot}$)	m_{DM} ($10^5 M_{\odot}$)	$\epsilon_{\text{DM,stars}}$ (kpc h^{-1})
TNG50	51.7 ³	35	2160 ³	2160 ³	0.85	4.5	0.39 → 0.195
TNG50-Dark	51.7 ³	35	...	2160 ³	...	5.38	0.39 → 0.195

Note. Parameters shown are the simulation volume, side length of the box, numbers of gas and DM particles, target baryon and DM masses, and $z = 0$ Plummer (equivalent) gravitational softening of DM and stars.

while $T \geq 0.66$ implies a prolate ellipsoid. Finally, triaxial ellipsoids are those in the range $0.33 \leq T \leq 0.66$. Observational estimates (Ravindranath et al. 2006; Van der Wel et al. 2014; Zhang et al. 2019) indicate that galaxies tend to be elongated at low stellar mass and high redshifts, and are more disk-like at higher stellar mass and low redshifts.

Theoretically, there have been many works trying to estimate the shape of DM halos using different techniques and simulations (Barnes & Efstathiou 1987; Dubinski & Carlberg 1991; Warren et al. 1992; Dubinski 1994; Eisenstein & Loeb 1995; Thomas et al. 1998; Prada et al. 2019; Jing & Suto 2002; Springel et al. 2004; Allgood et al. 2006; Tenneti et al. 2015; Butsky et al. 2016; Shao et al. 2020). While these studies confirm the triaxial nature of DM halos, their inferred shapes differ slightly.

Almost all of these studies ignore the impact of baryons in their shape estimation or just include adiabatic hydrodynamics. The general consensus is that the ratio of minor-to-major axes for DM halos, without baryonic effects included, is about $s = a/c = 0.5 \pm 0.2$ (see Springel et al. 2004 and references therein). Furthermore, we may expect that the DM halo shape in this case depends on the angular momentum of halo mergers.

Including baryonic effects, such as gas cooling (Kazantzidis et al. 2004) and star formation, is much more demanding. It is believed that these effects would “round up” the galaxies and make a transition from a prolate halo to a more oblate/spherical one. Kazantzidis et al. (2004) showed that gas cooling leads to an average enhancement of principal axis ratios by an amount of order $\simeq 0.2$ – 0.4 . There have also been several works trying to model the potential and shape of the MW halo, in particular by using stellar streams. For example, Abadi et al. (2010) investigated the radial dependence of halo shapes inside their hydrodynamical simulations and found $s = a/c \sim 0.85$. On the other hand, Law & Majewski (2010) estimated $a/c \simeq 0.72$ and $b/c \simeq 0.99$. Another interesting quantity in this context is the alignment of the angular momentum of the galaxy with the minor axis. Bailin & Steinmetz (2005) found a mean misalignment of order $\simeq 25^\circ$. Chua et al. (2019) used the Illustris simulation and showed a median of $s \simeq 0.7$ for halo masses $M \leq 10^{12.5} M_{\odot}$. Prada et al. (2019) used AURIGA simulations to infer DM halo shape and demonstrated that baryonic effects make DM halos rounder at all radii than dark matter only (DMO) simulations (Zhu et al. 2016).

There are also some studies (for example, Pandya et al. 2019 and references therein) that try to use the elongation of low-mass galaxies to shed light on the cosmic web at high redshifts.

In this paper, we build on previous investigations and use TNG50 (Pillepich et al. 2019; Nelson et al. 2019), a very high-resolution hydrodynamical simulation that simultaneously evolves dark and baryonic matter in a cosmological volume. We estimate the shape of DM halos for a sample of 25 MW-like galaxies. We use three different approaches in calculating

the shape parameters. Our main algorithm is based on the standard enclosed volume iterative method. We also infer the shape using a local shell non-iterative method as well as a local shell iterative method. We compare the radial profile of shape parameters in these approaches at the level of median and percentiles. We classify halos into three different categories. Simple, twisted, and stretched halos present different features in the radial profile of their axis lengths as well as in the level of alignment of axes between different radii. We make a comprehensive exploration of different halos and connect the shape with different halo properties as well as with the satellites of the halo. To seek the impact of the baryonic effects, we study DMO simulations with no baryons. Finally, we study the connection of these theoretical results and some recent observations.

The paper is organized as follows. Section 2 reviews the simulation setup. Section 3 presents different algorithms in computing the DM halo shape. Section 4 focuses on the shape analysis. Section 5 discusses the main drivers of the shape. Section 6 studies the connection with observations. Section 7 presents the summary of results. Some of the technical details such as non-disk-like galaxies and a convergence check are left to Appendices A–D.

2. Methodology and Definitions

2.1. TNG50 Simulation

TNG50, the third in the series of IllustrisTNG simulations, refers to the highest-resolution realization of large-scale hydrodynamical cosmological simulations (Pillepich et al. 2019; Nelson et al. 2019) and provides a remarkable combination of volume and resolution as listed in Table 1. As a hydrodynamical cosmological simulation, it evolves gas, DM, SMBHs, stars, and magnetic fields within a periodic-boundary box. The softening length is 0.39 comoving kpc h^{-1} for $z \geq 1$ and 0.195 proper kpc h^{-1} for $z < 1$.

Its initial conditions have been chosen from a set of 60 realizations of the initial random density field at $z = 127$ and using the Zeldovich approximation. The choice of its cosmological parameters is based on Planck Collaboration et al. (2016) with the following parameters: $\Omega_m = \Omega_{\text{dm}} + \Omega_b = 0.3089$, $\Omega_b = 0.0486$, $\Omega_{\Lambda} = 0.6911$, $H_0 = 100 h \text{ km s}^{-1} \text{ Mpc}^{-1}$, $h = 0.6774$, $\sigma_8 = 0.8159$, and $n_s = 0.9667$. The above initial conditions have been evolved using the AREPO code (Springel 2010), which solves a set of coupled equations for the magnetohydrodynamics (MHD) and self-gravity. Poisson’s equations for gravity are solved using a tree-particle-mesh algorithm.

Models for unresolved astrophysical processes, such as star formation, stellar feedback, and SMBH formation, growth, and feedback, used in TNG50 are the same as for the other

IllustrisTNG simulations and are described in detail in Weinberger et al. (2017) and Pillepich et al. (2018).

2.2. Milky Way-like Galaxies

Halos in TNG simulations are identified using a friends-of-friends (FoF) group finder algorithm (Davis et al. 1985). Furthermore, gravitationally self-bound subhalos are determined based on the SUBFIND algorithm (Springel et al. 2001; Dolag et al. 2009). Every FoF has one central galaxy, the most massive subhalo, and a number of satellites. Here we limit our study to central subhalos with masses in the range $(1-1.6) \times 10^{12} M_{\odot}$, which is the halo mass range appropriate to Milky Way-like galaxies (Posti & Helmi 2019). There are 71 galaxies in TNG50 within the above selection criterion. Furthermore, below we add an extra selection criterion and choose disk-like galaxies from the above sample. This is motivated by the fact that observations of the local universe show that massive star-forming galaxies, such as the MW, present a disk-like shape (Schinnerer et al. 2013). As described in the following, our selection is based on the orbital circularity parameter.

Galaxies in the TNG simulation are split into cases with dominant rotationally supported disks and isotropic bulge-like shapes. Throughout this work, we are mostly interested in the former case. In the following, we describe an algorithm to identify rotationally supported stellar components. Our formalism is based on Abadi et al. (2003) and El-Badry et al. (2018).

First, we calculate a galaxy’s stellar net specific angular momentum vector, \mathbf{j}_{net} :

$$\mathbf{j}_{\text{net}} \equiv \frac{\mathbf{J}_{\text{tot}}}{M} = \frac{\sum_i m_i \mathbf{r}_i \times \mathbf{v}_i}{\sum_i m_i}, \quad (1)$$

where the index i refers to star particles. Conventionally, the z axis points in the \mathbf{j}_{net} direction.

Next, for every star particle, we calculate the component of its angular momentum along the z direction, pointing in the direction of \mathbf{j}_{net} :

$$j_{z,i} = \mathbf{j}_i \cdot \hat{\mathbf{z}}, \quad \hat{\mathbf{z}} \equiv \frac{\mathbf{j}_{\text{net}}}{|\mathbf{j}_{\text{net}}|}, \quad \mathbf{j}_i = \mathbf{r}_i \times \mathbf{v}_i. \quad (2)$$

Finally, we define the orbital circularity parameter as the ratio between $j_{z,i}$ and $j_c(E_i)$ (which is the specific angular momentum of the i th star particle in a circular orbit, with radius r_c , and with the same energy as E_i):

$$\varepsilon_i \equiv \frac{j_{z,i}}{j_c(E_i)}, \quad j_c(E_i) = r_c v_c = \sqrt{GM(\leq r_c) r_c}. \quad (3)$$

For every particle, we compute the radius of the circular orbit by equating the particle’s energy with the specific energy of a circular orbit $E(r_c) = GM(\leq r_c)/2r_c + \phi(r_c)$ where $M(\leq r_c)$ refers to the mass interior to the circular orbit. $\phi(r_c)$ refers to the radial profile of an averaged gravitational potential for a collection of stars, gas, DM, and central BH in some radial bins within the galaxy. To compute $\phi(r_c)$ we divide the radial distance (from the center) to many different bins and compute the averaged total potential at every location.

Since the circular orbit has the largest angular momentum, we have $|\varepsilon_i| \leq 1$ with positive/negative values for prograde/retrograde orbits, while $\varepsilon_i = 0$ for radial or isotropic orbits, i.e.,

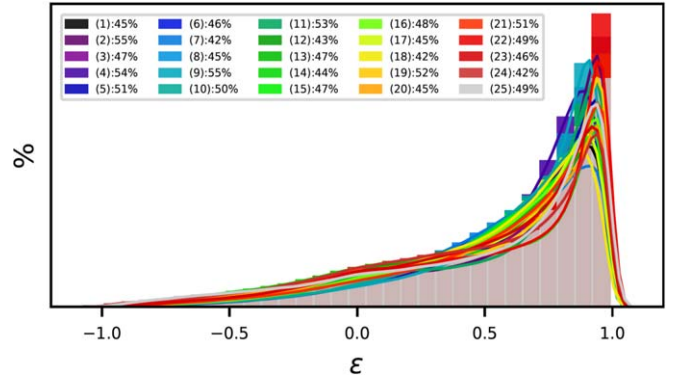


Figure 1. Probability density of orbital circularity parameter, ε , for a sample of 25 MW-like galaxies in TNG50 simulation labeled according to Disk-frac. Different colors describe various galaxies.

bulge-like components. We identify the stellar disk as those star particles with $\varepsilon_i \geq 0.7$, where hereafter we remove the index i for brevity. Furthermore, we limit our searches to cases with a fraction of stars in the disk (hereafter Disk-frac), defined with $\varepsilon \geq 0.7$, above 40% located at a radial distance of less than 10 kpc from the center. This ensures that we have a reasonable fraction of stars in the disk. This criterion reduces the sample to 25 galaxies in TNG50. Figure 1 presents the distribution of ε for the sample of MW-like galaxies. The dominant prograde orbit of stars is evident from the figure. About 72% of these galaxies have Disk-frac between 40% and 50%, while 28% have Disk-frac between 50% and 60%. Since the distribution of orbital circularity parameter has a similar profile in our samples, it is intriguing to see what the object-to-object variation in Disk-frac will be for real galaxies. In order to facilitate the presentation of different galaxies, in Table 2 we order subhalos and link their ID with a number from 1 to 25. Below we use these numbers instead of halo ID number for brevity.

To get an idea of what different galaxies in our sample look like, in Figure 2 we present synthetic images (using Pan-STARRS1 g, r, i filters) for a subset of our sampled MW-like galaxies. The images are taken from the TNG50 Infinite Gallery⁷ at $z = 0.05$ and are matched to our galaxy samples at $z = 0$ using merger trees. Each image is generated using the SKIRT radiative transfer code (Camps & Baes 2015) and includes the impact of dust attenuation and scattering (Rodríguez-Gomez et al. 2019). Text labels indicate the total stellar mass as well as the 3D stellar half-mass radius.

Although from Figure 1 the distribution of orbital circularity parameter is fairly similar in all of the galaxies in our sample, their synthetic images show clear morphological differences. It is therefore intriguing to see how the shapes of DM halos differ between these samples.

Before we proceed with the analysis of DM halo shapes, in Figure 3 we analyze the logarithm of 2D projected (number) density of DM particles, in the x - y plane, in a set of four MW-like galaxies from our sample. Our chosen halos are the same as those in Figure 2. Each row presents one galaxy, with a given ID number, and from left to right we zoom in further down to the central part of the halo. It is seen from the plot that halo structures vary. Moreover, in the second row, we see a ghost of a substructure that was imperfectly subtracted from the central halo.

⁷ www.tng-project.org/explore/gallery/rodriguezgomez19b/

Table 2
Link Between Subhalo ID and Halo Number in MW-like Galaxies

1 \mapsto 476266	2 \mapsto 478216	3 \mapsto 479938	4 \mapsto 480802	5 \mapsto 485056
6 \mapsto 488530	7 \mapsto 494709	8 \mapsto 497557	9 \mapsto 501208	10 \mapsto 501725
11 \mapsto 502995	12 \mapsto 503437	13 \mapsto 505586	14 \mapsto 506720	15 \mapsto 509091
16 \mapsto 510585	17 \mapsto 511303	18 \mapsto 513845	19 \mapsto 519311	20 \mapsto 522983
21 \mapsto 523889	22 \mapsto 529365	23 \mapsto 530330	24 \mapsto 535410	25 \mapsto 538905

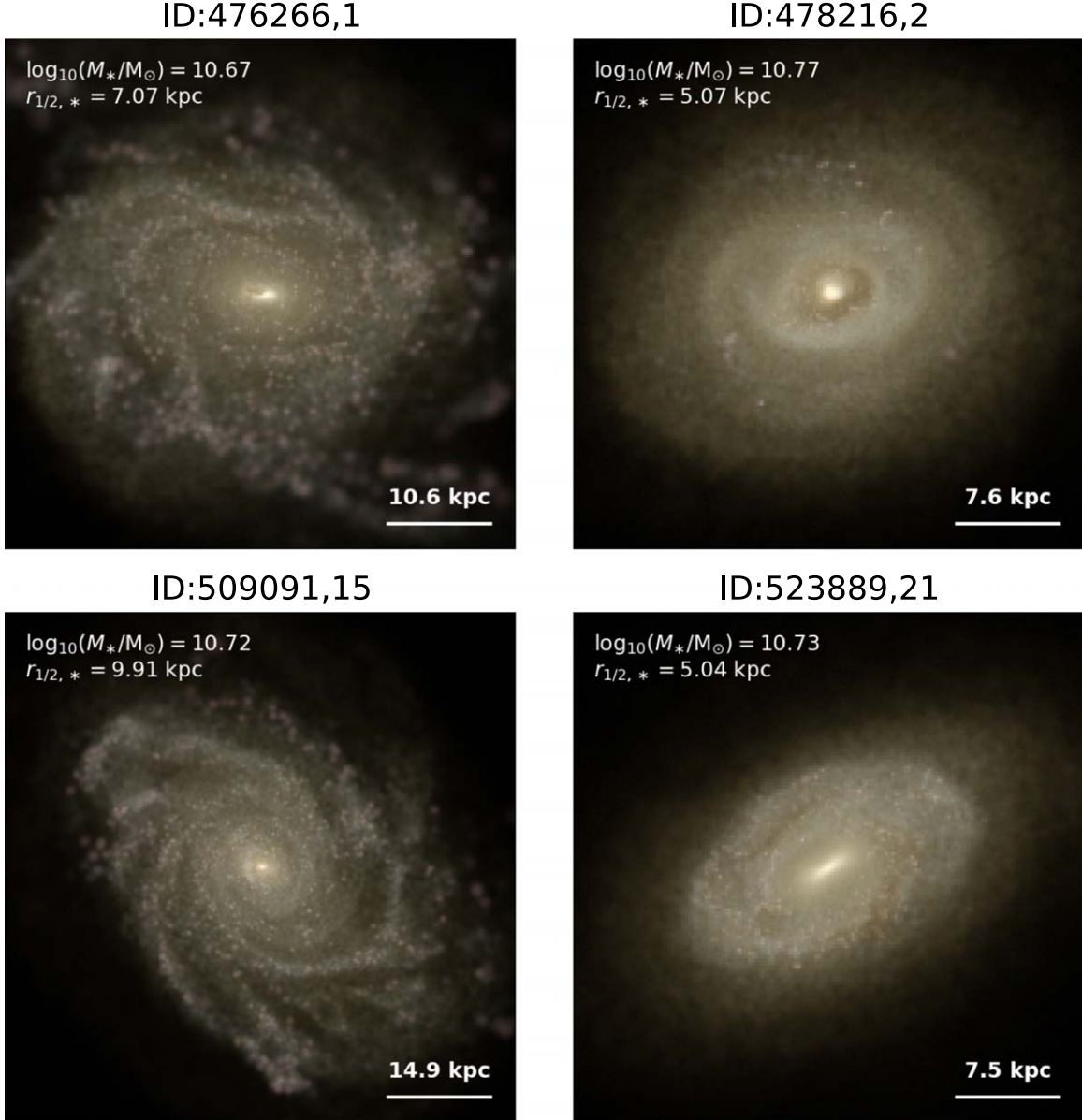


Figure 2. Synthetic images of a subset of our sampled MW-like galaxies from TNG50 simulation. Images are generated from the SKIRT radiative transfer code and using Pan-STARRS1 g, r, i filters.

Below we compute the shape for the above sample of (25 MW-like) galaxies using different techniques. We start by presenting these methods in detail and then infer the shape of dark matter halo accordingly.

3. Different Algorithms in Shape Analysis

Having presented the orbital circularity parameter as a key to identifying rotationally supported MW-like galaxies, we turn our attention to DM halo shape. There are different approaches in the literature to computing the galaxy shape (see, e.g.,

Schneider et al. 2012; Gómez et al. 2017; Chua et al. 2019; Monachesi et al. 2019, and references therein). Below we compute the DM halo shape using different methods. While the main focus of our analysis is on a generalization of the method of Schneider et al. (2012), in Section 3.2 we adopt the algorithm of Monachesi et al. (2019) and analyze the shape using a non-iterative local shell method. We compare their final results with ours. To facilitate reference to these methods, hereafter we name the former method the enclosed volume iterative method (EVIM) and the latter the local shell non-iterative method (LSNIM).

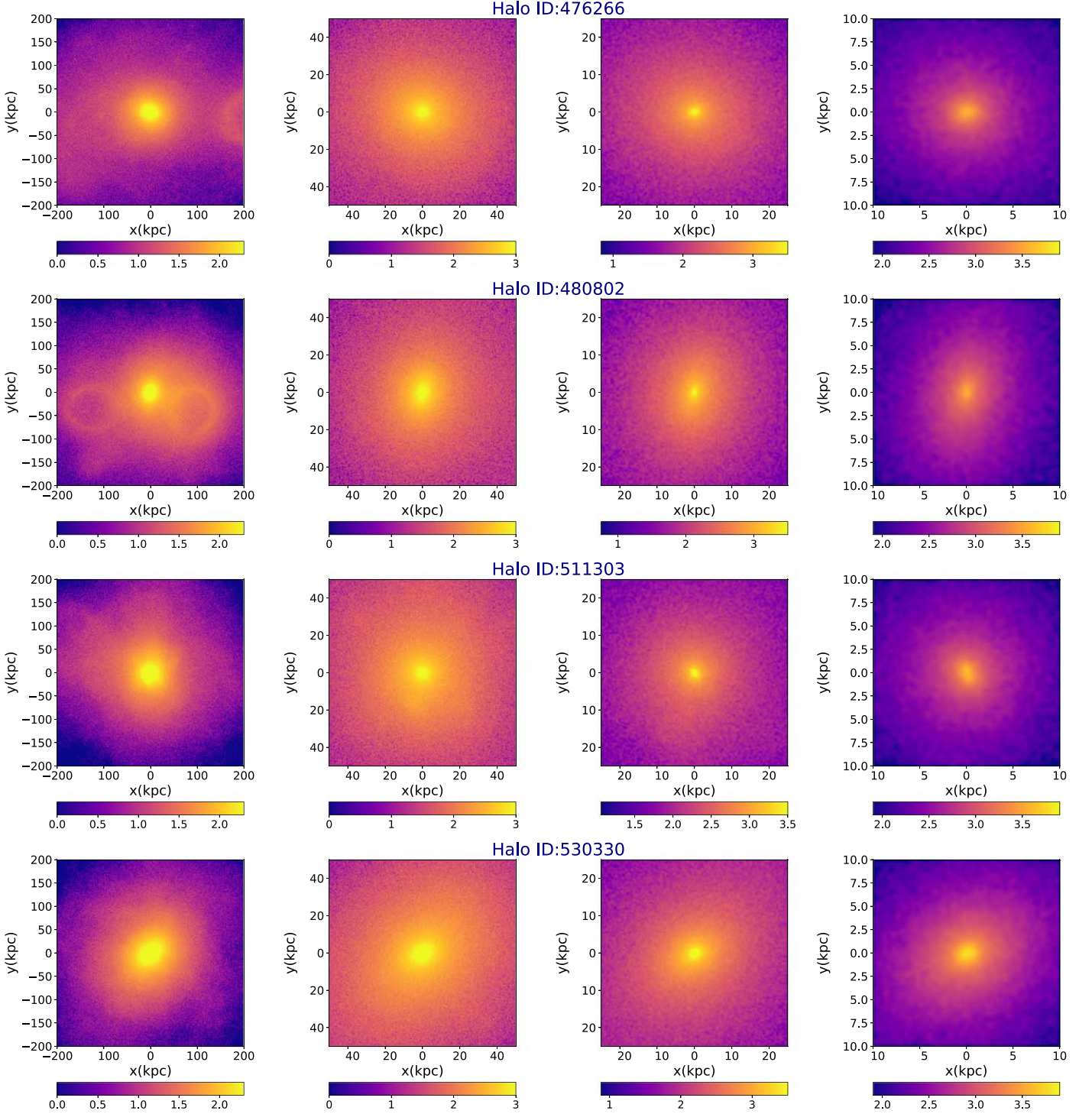
$\log_{10}(n/kpc^2)$ DM Halo


Figure 3. Logarithm of the projected number density of DM particles in a subsample of MW-like galaxies. The halo ID is mentioned on the top of each row. The color bars indicates the projected number density of DM particles.

3.1. Enclosed Volume Iterative Method

Our main method for shape analysis relies on the standard algorithm presented in Schneider et al. (2012). Given the triaxial nature of DM halos, we estimate the shape using the axis ratios of a 3D ellipsoid.

We split the interval from $r_{\text{sph}}^i = 2$ kpc to $r_{\text{sph}}^e = 202$ kpc into $N = 100$ logarithmic radial bins, and within each radius we

compute the reduced inertia tensor:

$$I_{ij}(\leq r_{\text{sph}}) \equiv \sum_{n=1}^{N_{\text{part}}} \frac{x_{n,i}x_{n,j}}{R_n^2(r_{\text{sph}})}, \quad i, j = 1, 2, 3, \quad (4)$$

where N_{part} refers to the total number of DM particles interior to an ellipsoid with the axis lengths $a(r_{\text{sph}})$, $b(r_{\text{sph}})$, $c(r_{\text{sph}})$.

Here, $x_{n,i}$ describes the i th coordinate of the n th particle. Furthermore, $R_n(r_{\text{sph}})$ denotes the elliptical radius of the n th particle, defined in terms of the halo axis lengths as

$$R_n^2(r_{\text{sph}}) \equiv \frac{x_n^2}{a^2(r_{\text{sph}})} + \frac{y_n^2}{b^2(r_{\text{sph}})} + \frac{z_n^2}{c^2(r_{\text{sph}})}. \quad (5)$$

In this method, our shape computation is based on an iterative approach partially owing to the fact that the elliptical radius contains the axis lengths ($a(r_{\text{sph}})$, $b(r_{\text{sph}})$, $c(r_{\text{sph}})$), which are unknown a priori. We shall then determine them in a few steps by using an iterative method. At any radius, we iteratively compute the reduced inertia tensor starting with all the particles within a sphere of radius r_{sph} . The eigenvalues and eigenvectors of the diagonalized inertia tensor are then used to deform the initial sphere (from the ellipsoid from the second step) while keeping the interior volume fixed. This requires a rescaling of the inferred halo's axis lengths from $a = \sqrt{\lambda_1}$, $b = \sqrt{\lambda_2}$, and $c = \sqrt{\lambda_3}$ to

$$\begin{aligned} a &= \frac{r_{\text{sph}}}{(abc)^{1/3}} \sqrt{\lambda_1}, \\ b &= \frac{r_{\text{sph}}}{(abc)^{1/3}} \sqrt{\lambda_2}, \\ c &= \frac{r_{\text{sph}}}{(abc)^{1/3}} \sqrt{\lambda_3}, \end{aligned} \quad (6)$$

where λ_i ($i = 1, 2, 3$) refers to the eigenvalues of the inertia tensor. Hereafter we skip showing the radial dependence of a , b , and c for brevity. Since the eigenvectors of the inertia tensor give us the principal axes, we rotate all the DM particles to the frame of the principal axes as the coordinate system defined with the basis vectors along with the eigenvectors. The only thing to check is that they constitute a right-handed set of coordinates. At every step, the halo shape is computed as the ratio of the minor-to-major axes, $s = a/c$, and the ratio of the intermediate to major axes, $q = b/c$.

The iteration process is terminated when the residual of both s and q converges to a level below $\max(((s - s_{\text{old}})/s)^2, ((q - q_{\text{old}})/q)^2) \leq 10^{-3}$, where \max refers to the maximum between the two quantities. In Appendix B we present the algorithm in more detail. After the convergence is established, we also compute the angle between the eigenvectors of the inertia tensor and the total angular momentum of the disk.

3.2. Local Shell Non-iterative Method

Our second approach in computing the halo shape is based on the algorithm of Monachesi et al. (2019). In this method, the interval from $r_{\text{sph}}^i = 2.0$ kpc to $r_{\text{sph}}^e = 202$ kpc is divided into 40 spherical shells and we compute the shape for every shell. In addition, we use an unnormalized inertia tensor:

$$\mathcal{M}_{ij} = \sum_{n=1}^{N_{\text{shell}}} x_{n,i} x_{n,j}, \quad (7)$$

where N_{shell} represents the total number of particles (of interest) within the shell. Finally, $x_{n,i}$ describes the i th component of the n th particle. Since the particles are considered in spherical shells and as the inertia tensor is not weighted with the elliptical axes, the shape is computed in one step and without any

iterations. The above inertia tensor is computed for every spherical shell, with radii r_i and r_{i+1} from the above interval, and is then diagonalized to find the eigenvalues. In addition, since the shells are not deformed, there is no need to rescale the eigenvalues, and the halo axis lengths are simply the square root of the eigenvalues. We shall emphasize here that LSNIM is presented only for comparison and we take EVIM as our main approach throughout the subsequent analysis.

3.3. Local Shell Iterative Method

Our third method in analyzing the halo shape relies on a local shell iterative method (LSIM). In this approach, we construct 100 algorithmic radial thin shells in the interval from $r_{\text{sph}}^i = 2$ kpc to $r_{\text{sph}}^e = 202$ kpc and calculate the reduced inertia tensor using Equation (4), with the main difference that we replace the interior interval with particles located in thin local shells. At each radius, we iteratively compute I_{ij} in the above shells with an initially spherical shape $a = b = c = r_{\text{sph}}$ that is distorted iteratively until when the method converges. In a manner similar to EVIM, we compute the eigenvalues and eigenvectors of the localized inertia tensor and deform the shells. Also, to control the deformed ellipsoids locally, at every radius, we take the enclosed volume to be fixed. The remaining steps are quite similar to EVIM. Chua et al. (2019) adopted an approach somewhat similar to LSIM in their shape analysis. However, in their analysis, they adopted a weighting factor of unity. While we do not expect this to change the picture for thin shells, in Appendix D we check this more explicitly and compute the shape parameters using LSIM with two different weighting factors—1 versus r^{-2} . We find that the final results are relatively insensitive to the choice of weight.

We adopt EVIM as the main method in our analysis, but we also compare its outcome to those of LSNIM and LSIM in several places in this work.

4. Shape Profile Analysis

Before we proceed with analyzing individual halos using EVIM, we study the shape profiles at the level of the median/percentiles.

4.1. Statistical Shape Analysis

Figure 4 presents the radial profile of the median and 16 (84) percentiles of (s, q, T) inferred from EVIM, LSNIM, and LSIM. From the plot, we can infer several interesting features.

1. The radial profile of the s parameter is fairly similar between EVIM and LSIM in the inner part of the halo but deviates slightly beyond a radius of 80 kpc. In contrast, LSNIM predicts a larger profile for the s parameter, which is progressively diminishing from the inner to the outer part of the halo.
2. The inferred radial profile of the q parameter is very close between EVIM and LSIM up to a radius of 10 kpc. However, they start deviating from each other after this radius and then EVIM gets closer to LSNIM while LSIM decreases further out.
3. Finally, the inferred radial profile of the triaxiality parameter is fairly close between LSIM and LSNIM in terms of its behavior and amplitude but slightly different from that of EVIM. More explicitly, while the local method predicts an increasing profile for T throughout the

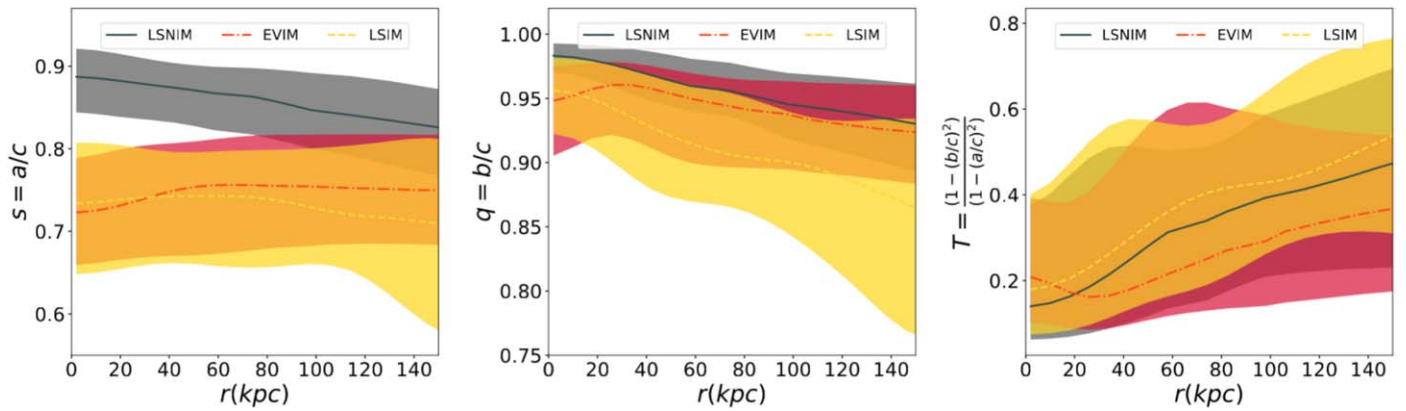


Figure 4. Comparison between the shape parameters s and q and triaxiality parameter T using the EVIM, LSNIM, and LSIM algorithms. The sample is stacked over 25 TNG50 galaxies.

Table 3

Median and 16th (84th) percentiles of DM halo shape parameters computed from EVIM, LSNIM, and LSIM

Method	s	q	T
EVIM	$0.752^{+0.062}_{-0.078}$	$0.944^{+0.022}_{-0.048}$	$0.236^{+0.307}_{-0.107}$
LSNIM	$0.864^{+0.034}_{-0.051}$	$0.956^{+0.022}_{-0.015}$	$0.346^{+0.227}_{-0.198}$
LSIM	$0.726^{+0.076}_{-0.073}$	$0.901^{+0.041}_{-0.049}$	$0.421^{+0.229}_{-0.181}$

halo, EVIM suggests a turnover behavior for T around 30 kpc.

- To make the comparison more robust, in Table 3 we present the median and 16th–84th percentiles of halo shape parameters estimated using the above three methods. Here the median and percentiles are computed in two steps. First we compute the radial profile of the median (percentile) using all galaxies in our sample and then we compute the median (percentile) along the radial direction and up to $r \simeq 200$ kpc. The results are rather close to each other. This indicates that the statistical behaviors of these approaches are fairly similar.

Quite interestingly, the median of the s parameter is very similar between the EVIM and LSIM and is smaller than for LSNIM. In contrast, the inferred median of q is closer between EVIM and LSNIM and is slightly larger than that of LSIM. Finally, the median of T is minimal from EVIM and is maximal from LSIM. Although these numbers are consistent with each other at the level of 16 (84) percentiles, it is interesting that the median itself shows some level of sensitivity to the actual method we use.

Finally, the comparison between LSIM and LSNIM is an interesting one. The fact that both s and q are smaller in LSIM than in LSNIM is intuitively understandable and is related to the fact that non-iterative methods generally predict a more spherical shape profile than iterative ones.

4.2. Halo-based Shape Analysis

Having presented a statistical analysis of halo shapes, in the following we analyze them individually. In addition, hereafter we take EVIM as the main algorithm in our shape analysis. To get a sense of how the results may depend on the actual method, in Appendix C we compare the shape parameters using EVIM with those using LSIM. This comparison demonstrates a fair agreement between the results and the halo

classifications. Therefore, as already stated above, we use EVIM in our subsequent halo classification.

Based on our shape analysis, we place DM halos in our galaxy sample into three main categories: (i) simple, (ii) twisted, and (iii) stretched halos. Halos in different classes behave differently in terms of their axis lengths and their orientation. Below we introduce these categories and describe each of them in some depth.

4.2.1. Simple Halos

We start by analyzing the simple halos in our galaxy sample. Based on EVIM, such halos have two main properties: first, they have three well separated eigenvalues such that the ordering in their magnitude does not change with radius; second, the eigenvector associated with the smallest eigenvalue is almost entirely parallel to the total angular momentum with little change in the angle. In addition, other eigenvectors present rather small directional variations as well. There are a total of eight halos in this category. In Appendix C.1, we present the radial profile of the axis lengths, as well as the angles of eigenvectors associated with the minimum (min), intermediate (inter), and maximum (max) eigenvectors with different fixed vectors: $L_{\text{tot}}^{\parallel}$ (the angular momentum of the stellar component of the galaxy) and three unit vectors along the x , y , z directions of the TNG simulation box (referred to as $[\hat{i}, \hat{j}, \hat{k}]$), and finally also the shape parameters s and q for this group.

Although we take EVIM as our main method, in Appendix C we inferred the shape profiles using both EVIM and LSIM to check the robustness of the properties of the simple halos against when different methods. It is generally true (with the exception of halo 511303) that the eigenvectors associated with the minimum eigenvalue are almost entirely parallel to the net angular momentum. However, owing to the local fluctuations, in some cases the lines do actually cross each other and a local rotation occurs. For that reason, we may call these halos simple/stretched but just refer to them as simple halos for short.

4.2.2. Twisted Halos

The second class of halos we analyze here is twisted halos. Halos in this category show some level of rotation in the radial profile of their eigenvectors. To demonstrate such rotation, we compute the angle of min, inter, and max eigenvectors with the

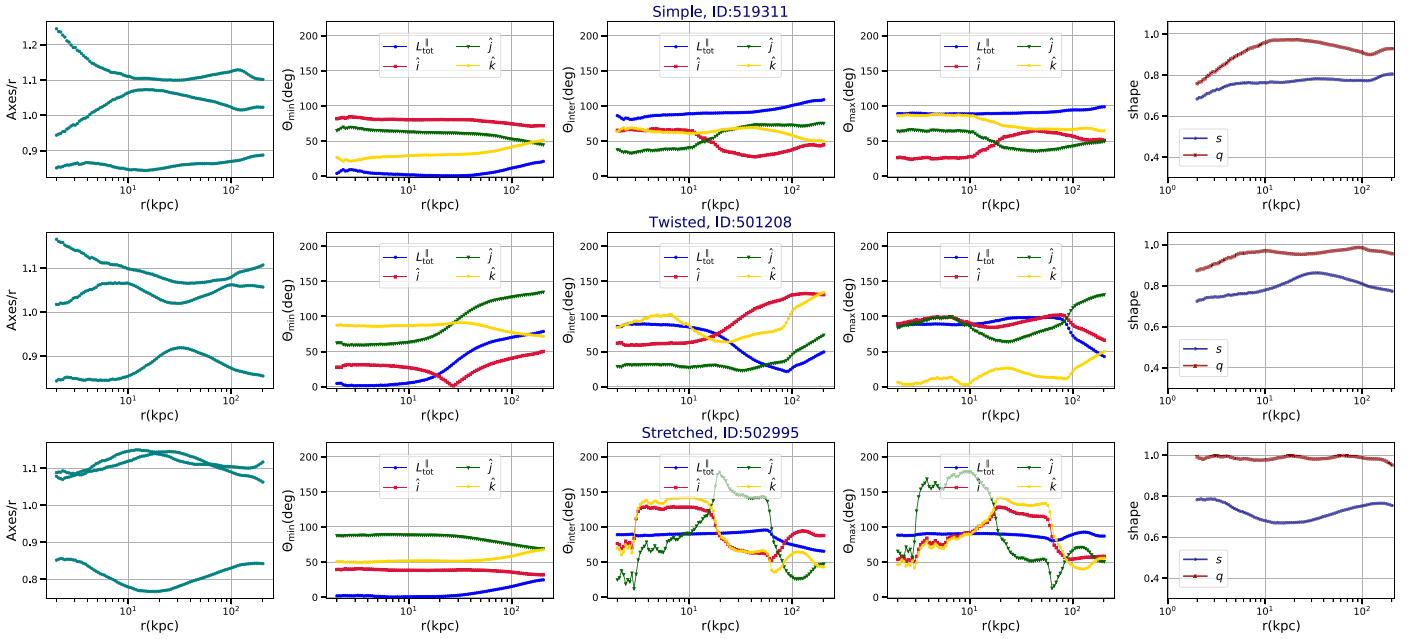


Figure 5. The radial profile of the axis lengths, angles of min, inter, and max eigenvectors with a few fixed vectors, $L_{\text{tot}}^{\parallel}$, \hat{i} , \hat{j} , and \hat{k} , and the shape parameters s and q for simple, twisted, and stretched halos. The simple halo (first row) presents a small rotation. The twisted halo (second row) shows some level of gradual rotation. The stretched halo (third row) establishes a rotation of about 90° when the axis lengths cross each other.

aforementioned fixed vectors in 3D such as $L_{\text{tot}}^{\parallel}$, \hat{i} , \hat{j} , and \hat{k} . Twisted halos experience a gradual rotation of about 50° – 100° in their radial profile. Furthermore, their axis lengths become very close to each other, sometimes at the crossing radius, but do not really get stretched, as is described below. There are eight halos in this class. In Appendix C.2 we summarize the radial profile of the axis lengths, different angles, and shape profile of all the twisted halos.

As was done in the case of simple halos, in Appendix C we overlay the shape parameters from LSIM. Generally speaking, the halo shapes inferred from EVIM and LSIM are fairly close to each other but only slightly noisier in LSIM because of the local fluctuations, which may lead to extra crossings of the eigenvalues.

4.2.3. Stretched Halos

The last class of halos we describe here is stretched halos. Generally speaking, halos belonging to this category experience a level of stretching in the radial profile of their axis lengths. Where two axis lengths approach each other, one of them stretches and becomes longer than the other. Thanks to the orthogonality of eigenvectors, such stretching can be easily seen by changing the angle of min, inter, and max eigenvectors with the aforementioned unit vectors ($L_{\text{tot}}^{\parallel}$, \hat{i} , \hat{j} , \hat{k}) by about 90° . Indeed, this criterion allows us to distinguish between twisted and stretched halos. In summary, the crucial difference between twisted and stretched halos is that the former establish a gradual change in their angle while the latter show a more abrupt change.

In our galaxy sample, we have nine halos in this category. In Appendix C.3 we summarize the radial profile of the axis lengths, different angles, and shape profile of all the stretched halos.

Before we proceed with further study of halo properties in different classes, we shall mention that there are two halos—halo 4 (ID: 480802) and halo 10 (ID: 501725)—that show both

a twisting and a stretching in their radial profiles at different radii. More explicitly, these halos demonstrate both a gradual change throughout their radial profiles and abrupt changes when the principal axis lengths cross each other. To avoid further complexity of the presentation, however, we place them in the category of stretched halos throughout our following analysis.

As for the above two cases, in Appendix C.3 we also overlay the shape profiles from the LSIM. Quite interestingly, the general patterns from EVIM and LSIM are fairly close to each other with extra fluctuations that arise owing to the local fluctuations of the profiles.

Having introduced different classes of halos, in Figure 5 we present three halos, one from each category, and compare the radial profile of their axis lengths, angles with different vectors, and their shape profiles. We use EVIM in our presentation. It is evident that the level of rotation in the simple halo is much less than in the twisted and stretched halos. In addition, while the twisted halo shows some level of gradual rotation throughout its radial profile, the stretched halo demonstrates a rotation of about 90° when the axis lengths cross each other.

4.3. 3D Visualization of Different Halos

Having specified different halo types in our galaxy sample, here we aim to make a 3D visualization of their ellipsoidal profiles. In Figures 6–8, we draw 3D ellipsoids of simple, twisted, and stretched halos at a few different locations. To make each plot, we have ordered the eigenvalues and made a rotation from the principal frame to Cartesian coordinates using the eigenvectors of the inertia tensor. In addition, for each plot, we also display the 2D projection of the 3D ellipsoid in the XY, YZ, and XZ planes. It is evident that while the simple halo presents very little rotation, the twisted and stretched halos establish some level of rotation. In addition, while the twisted halo presents a gradual rotation, the stretched halo establishes a larger rotation near the crossing of the axis lengths.

Simple, ID:519311

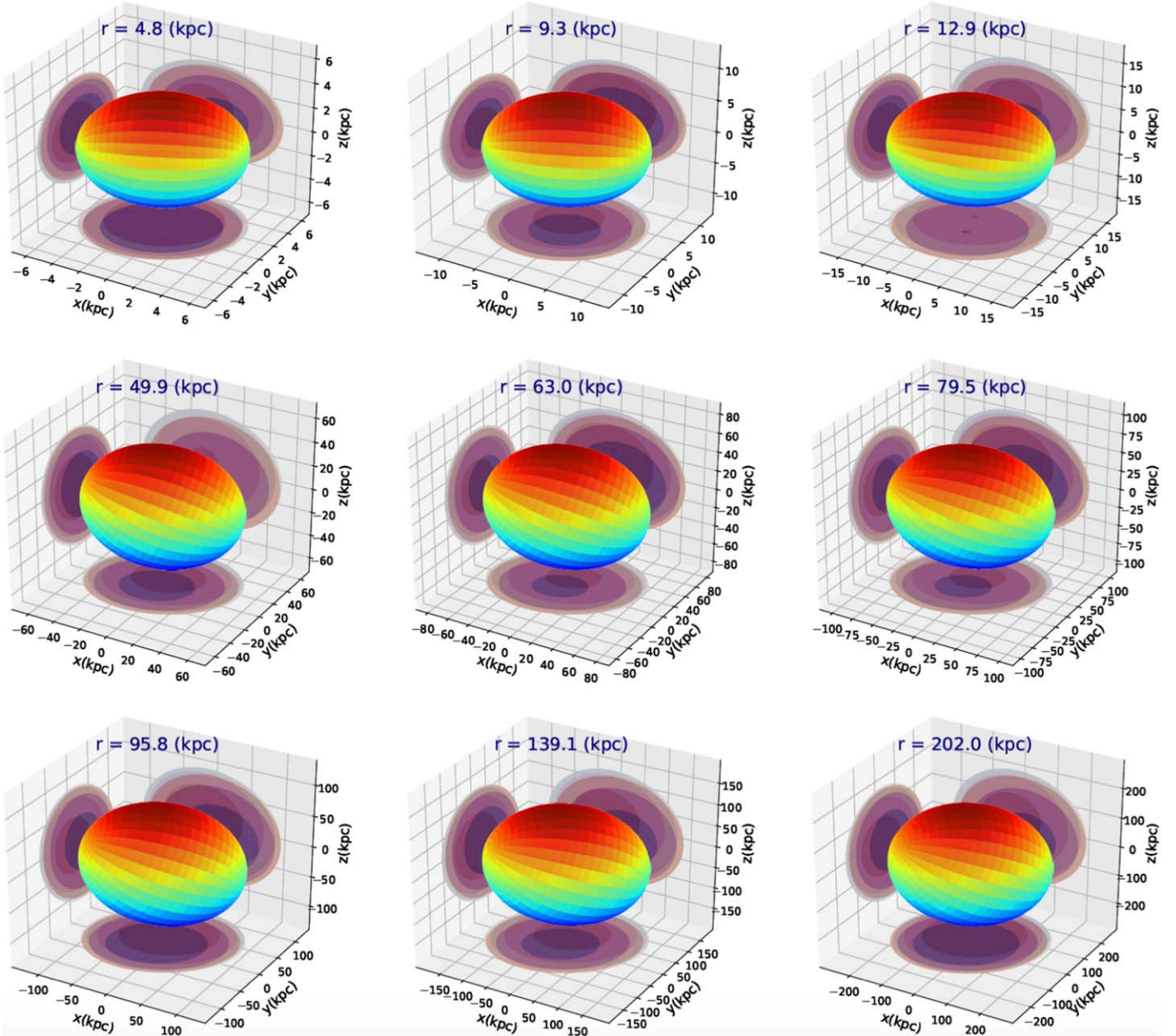


Figure 6. 3D ellipsoid for a simple halo. The halo experiences a rather weak level of rotation throughout its radial profile.

4.4. Halo Shape and Galaxy Properties

Having presented different halo types, below we make the connection between the shape of halos and various properties of a galaxy such as its stellar mass and the halo formation time.

4.4.1. Shape versus Central Galaxy Stellar Mass

Here we study the possible connection between the shape parameters and (central) galaxy stellar mass (hereafter galaxy stellar mass), M_* . Table 4 presents the Spearman correlation between the shape parameters at $r = 2r_{1/2,*}$ and galaxy stellar mass, where we have chosen a physical distance to draw a better connection with the halo mass.

Before drawing any conclusions from the table, we should point out that owing to the small sample of simple, twisted, and

stretched halos, care must be taken in interpreting the statistical significance of these correlations. To take this into consideration, we not only present the Spearman coefficient, Coeff , but we also report the p -value for every correlation. Furthermore, we name a correlation reliable if its p -value is less than 0.05. Having said this, it is clearly seen that only the correlation of q (T) and M_* for simple (twisted) halos is meaningful with a positive correlation. The correlation of T (q) and M_* for simple (twisted) halos are on the boundary of being reliable. However, the remaining correlations are not statistically reliable, having larger p -values.

In Figure 9, we find the correlation between $2r_{1/2,*}$ and M_* . From the plot, it is evident that stretched halos span a narrower range of radii while simple and twisted halos spread over a wider range of masses and radii.

Twisted, ID:501208

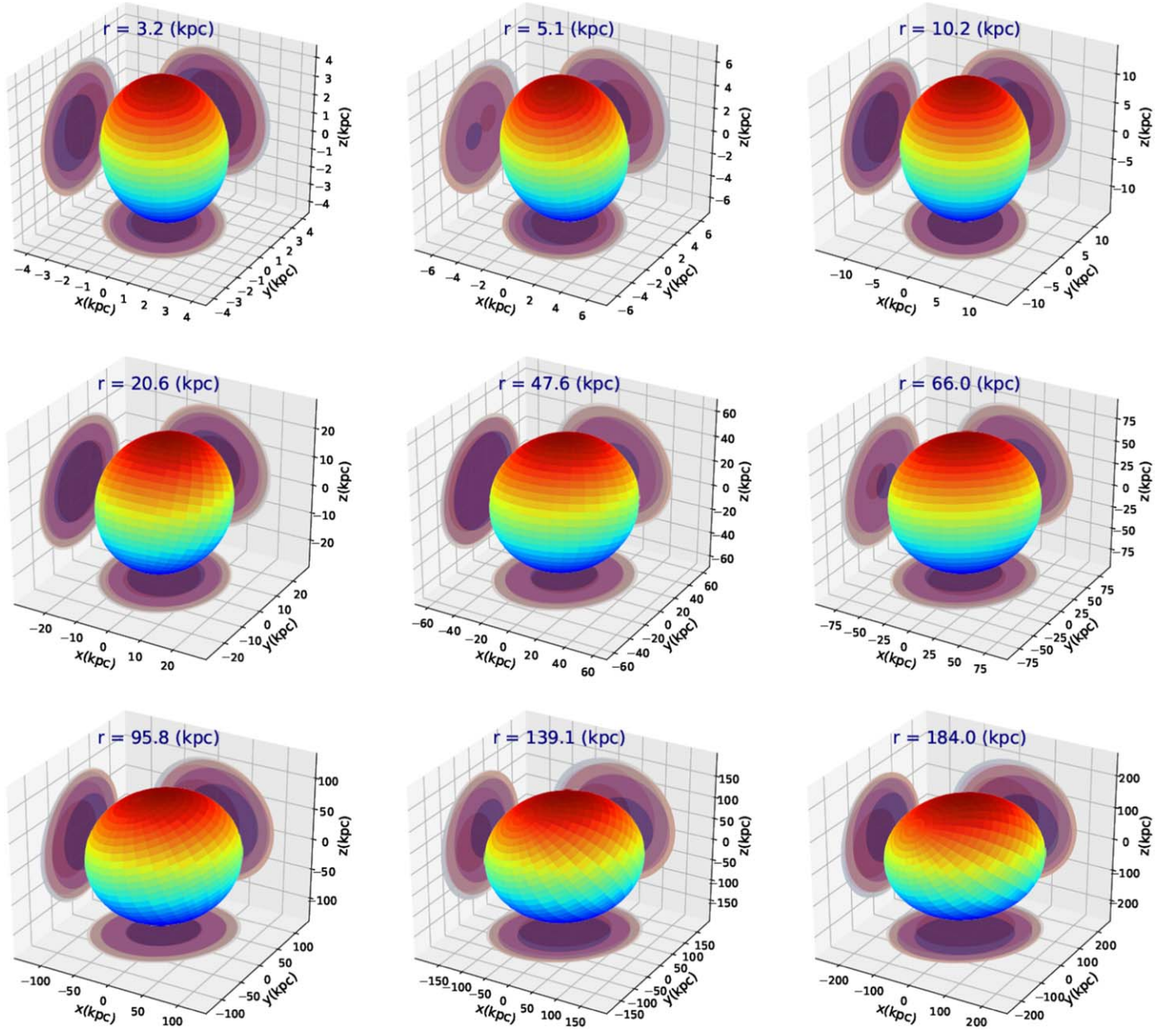


Figure 7. 3D ellipsoid for a twisted halo. The halo establishes some level of gradual rotation in its radial profile.

4.4.2. Shape versus (stellar) Halo Formation Time

Below, we make a possible connection between the shape parameters and the halo formation time ($z_{1/2,*}$), defined as the time when the half of the galaxy stellar mass has formed. Table 5 presents the Spearman correlation between (s , q , T) and $z_{1/2,*}$. As we already mentioned in the correlation of the shape parameters and M_* , care must be taken in drawing any meaningful conclusions about the real correlation because of the limited sample of halos in each category. Owing to this, we also report the p -value while presenting the correlation. As it turns out, the only meaningful correlation is between T and $z_{1/2,*}$ in the stretched halos. However, we should emphasize here that the sample of stretched halos is very limited with only five halos. Being aware of this caveat, we conclude that in our

galaxy samples, shape parameters do not seem to be correlated with the halo formation time.

Finally, it is interesting to make a possible connection between the halo mass and its formation time. Figure 10 presents the correlation between the galaxy stellar mass and the halo formation time. While the simple/twisted halos establish a positive correlation between M_* and $z_{1/2,*}$, stretched halos seem to indicate a rather flat correlation. Again we should keep in mind that the sample of stretched halos is rather limited. Therefore care must be taken in drawing any strong conclusions here. Being mindful of the statistical caveat here, it might be that the natures of different halo types are a bit different. This suggests us to use a larger box for TNG simulation and do the analysis for them as well. However, this is beyond the scope of this work and is left to future work. It is also

Stretched, ID:502995

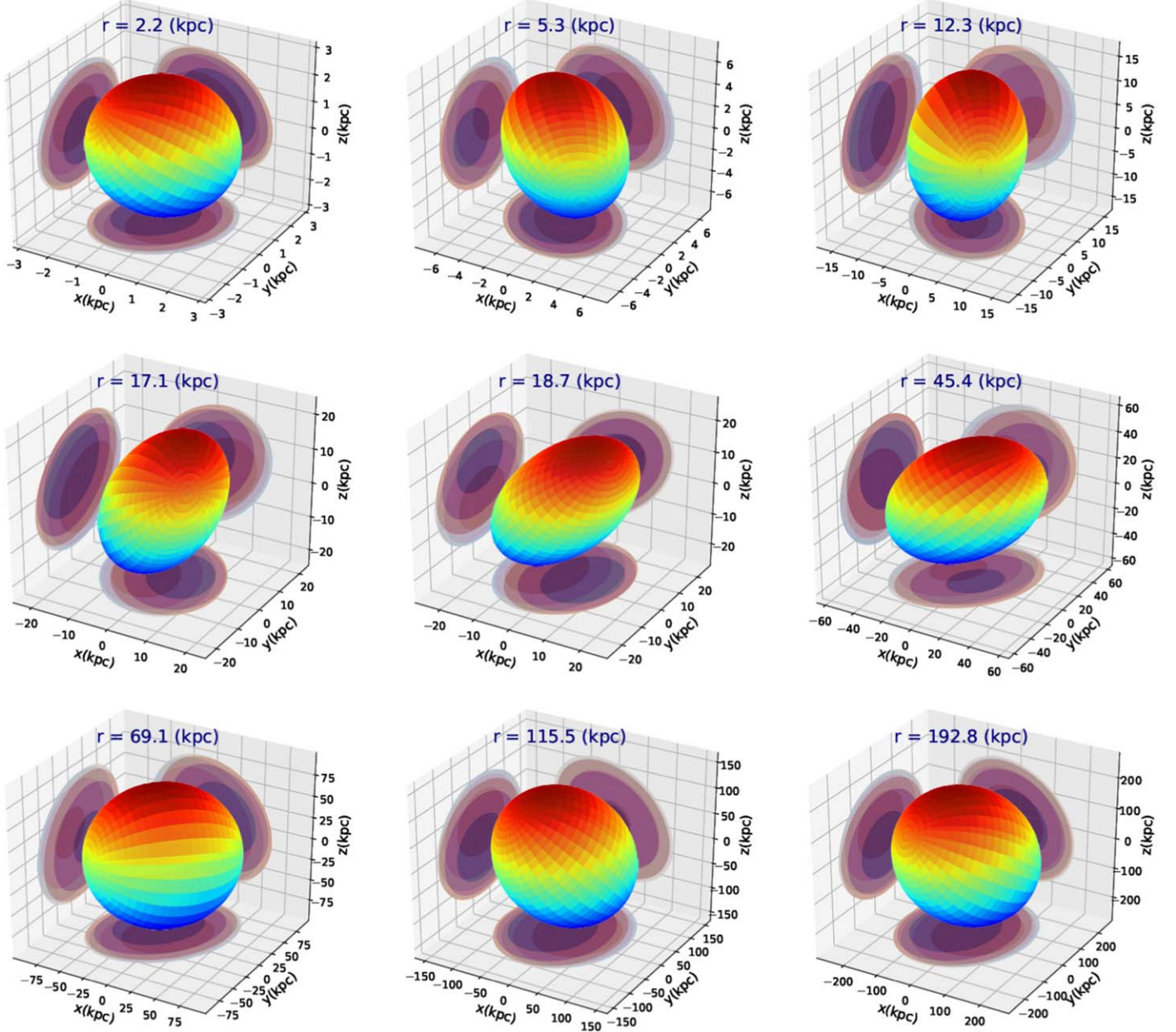


Figure 8. 3D ellipsoid for a stretched halo. The halo shows large levels of rotation in its radial profile very close to different crossings.

Table 4

Spearman Correlation between Shape Parameters (s, q, T) Located at $r = 2r_{1/2,*}$ and Galaxy Stellar Mass, M_*

		s	q	T
Simple	Coeff	-0.17	0.90	-0.71
	p -value	0.69	0.002	0.05
Twisted	Coeff	-0.17	0.57	-0.64
	p -value	0.69	0.14	0.09
Stretched	Coeff	-0.017	0.37	-0.28
	p -value	0.97	0.33	0.46

interesting to make a connection between the halo shape and the merger trees. We leave this investigation to future work as well.

5. Main Drivers of the Shape

Having computed the shape of the DM halo in MW-like galaxies, below we study the impact of a few different drivers of the shape. Here we mainly focus on three different drivers including baryonic effects and the impact of substructures on halo morphology. In addition, we find the connection between the angular momentum of satellites and the eigenvectors of the reduced inertia tensor as well as \mathbf{j}_{net} .

5.1. Baryonic Effects: DMO Simulations

One possible driver of DM halo shape is baryonic effects. Baryonic contributions are generally very complex and hard to account for individually, so in order to consider their possible impacts appropriately we compute the shape of DMO

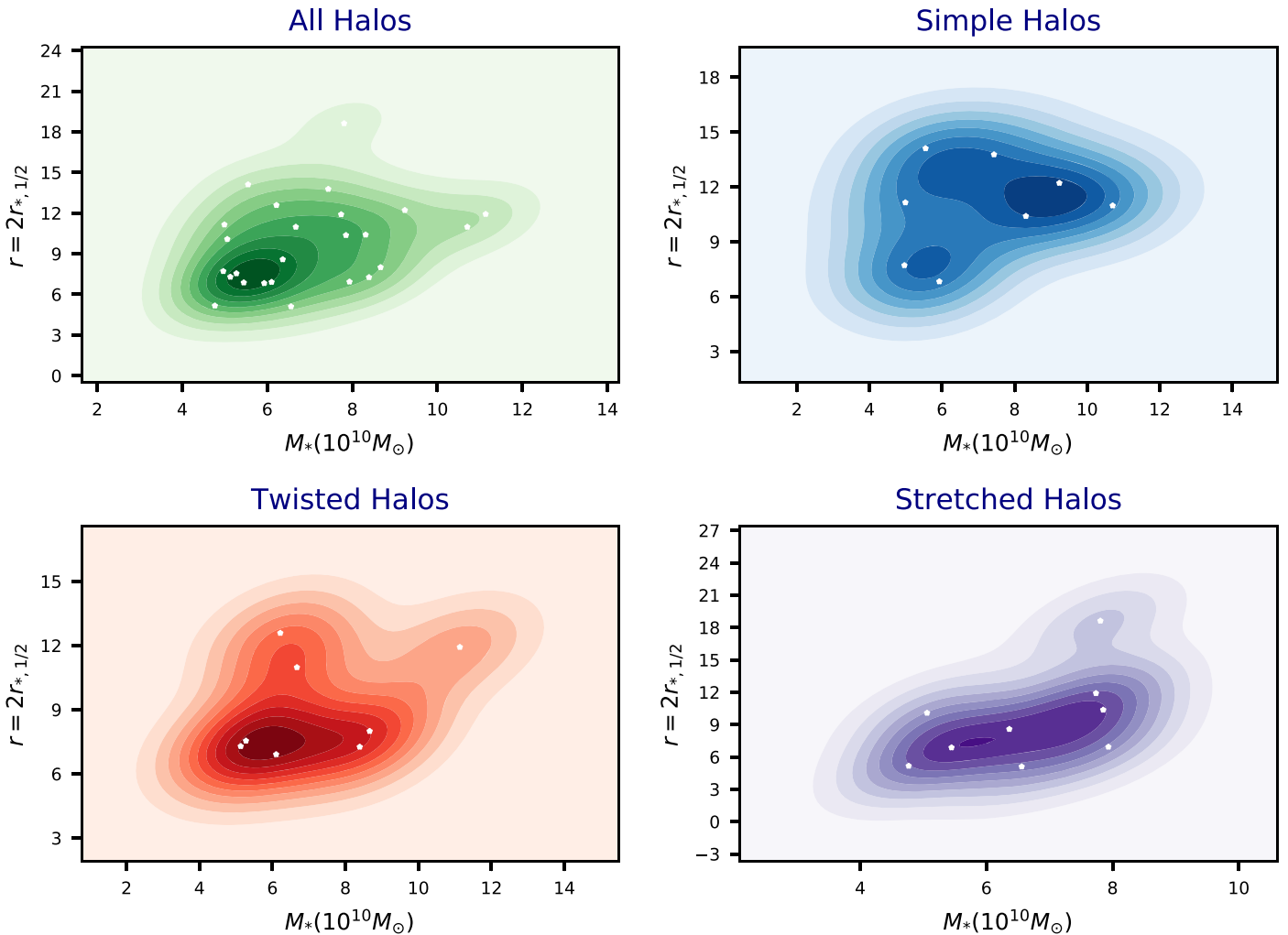


Figure 9. Correlation between the halo mass and half-mass radius. Stretched halos span a narrower range of radii while simple and twisted halos spread over a wider range of masses and radii and are a bit less compact. Dots in each panel refer to the individual halos.

Table 5

Spearman Correlation between the Shape Parameters (s , q , T) Located at $r = 2r_{1/2,*}$ and the Stellar Halo Formation Time, $z_{1/2,*}$

		s	q	T
Simple	Coeff	0.32	0.22	0.12
	p -value	0.43	0.61	0.78
Twisted	Coeff	0.048	-0.44	0.24
	p -value	0.91	0.27	0.57
Stretched	Coeff	0.45	-0.62	0.70
	p -value	0.23	0.07	0.04

simulations similar to Dubinski & Carlberg (1991), Warren et al. (1992), Jeon-Daniel et al. (2011), Schneider et al. (2012), and Chua et al. (2019). We then compare the final results with the estimated shape from the full hydrodynamical simulations.

We use TNG50-Dark and compute the shape of DMO MW-like halos. To match the halos from TNG50 to TNG50-Dark, we use the unique ID of dark matter particles. For every galaxy in our preselected sample, we scan the halos in DMO and look for the halo with the highest fraction of matched DM particles.

It is worth mentioning that TNG50 halos are less massive because of baryonic feedback processes, which eject some mass from the halo. This does not occur in the DMO simulation and thus halos in DMO are slightly more massive. To take this into account, in our matching, we take the mass range in TNG50-Dark to be slightly above the original selection in TNG50 because we have also put a prior choice on the range of halo mass to narrow down the interesting mass range a little. Therefore the matched DMO halos are found to be more massive; see Table 1 for more details. In most cases, the fraction of matched particles is more than 70%. In one case, though—the fourth galaxy in the above sample—the percentage of matched DM particles was about 54%.

Before proceeding with the shape analysis, in Figure 11 we study the logarithm of the 2D projected (number) density of DM particles, in the x - y plane, in a sample of four DMO halos of MW-like galaxies under consideration. Our chosen halos are associated with the cases matching those in Figure 3. Each row presents one galaxy, with its given ID number, and from left to right we zoom in further down to the central part of the halo. As expected, the halo structure for the DMO case varies from the DM profiles presented in Figure 3. Although all of the halos in our sample share the same gravity and subgrid baryonic

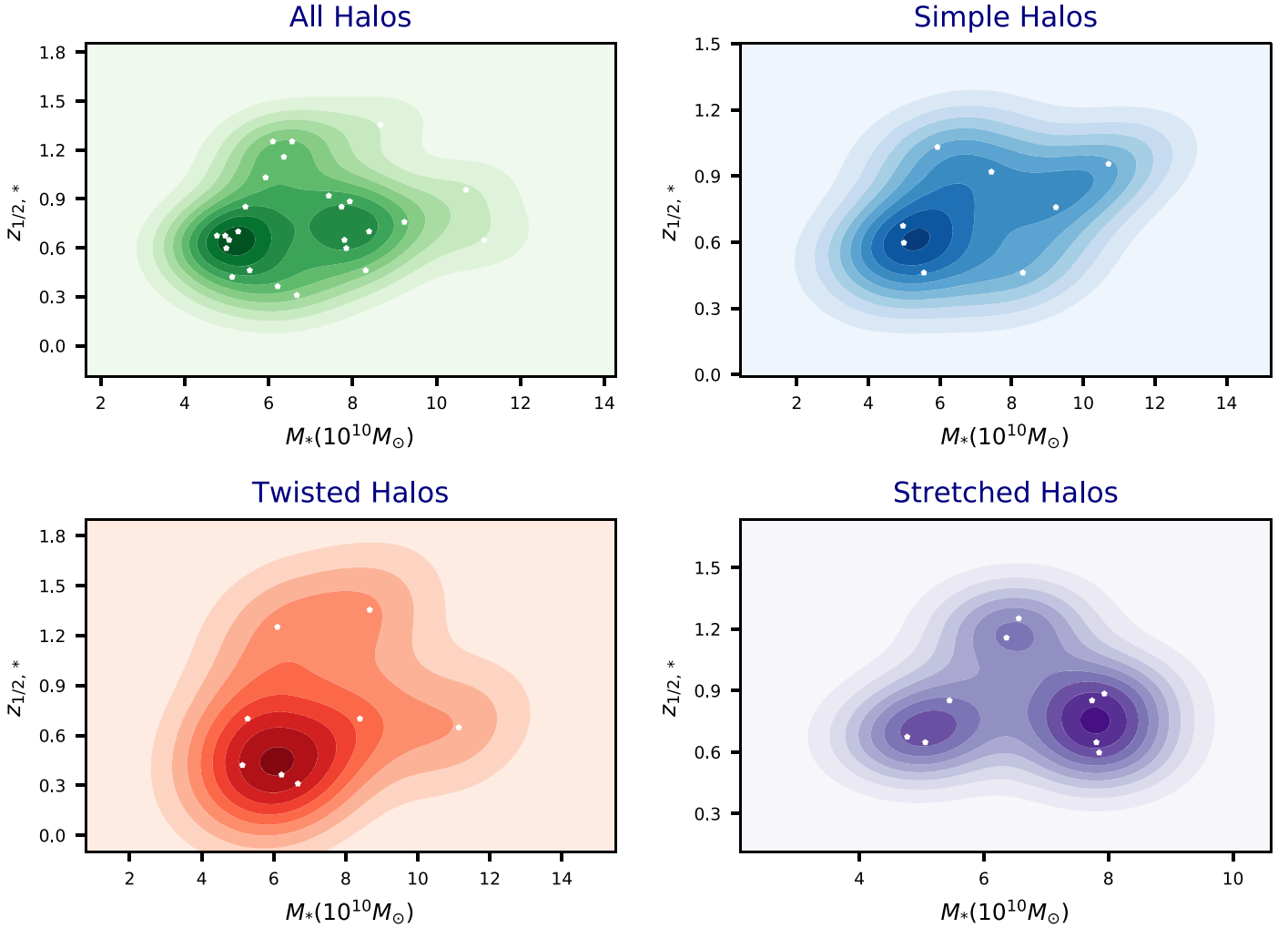


Figure 10. Correlation between the halo stellar mass and halo formation redshift. While both simple and twisted halos show some positive correlation between M_* and $z_{1/2,*}$, stretched halos establish a flat correlation. Dots in each panel refer to the individual halos.

physics, they differ in their formation histories. As a result of this, their density profiles differ. For example, the halo in the second row in Figure 3 is currently experiencing a halo merger.

In Figure 12 we draw the correlation between s and q (as inferred from EVIM) at $r = 0.1R_{200}$ for both TNG50 (Cen, left) and TNG50-Dark (DMO, right). To distinguish between the central halo and the FoF group that will be added later, we explicitly mention Cen here. Overlaid on each plot is the scatter plot of the same quantities in both cases. It is evident that, on average, central halos have larger values of s and q than DMO ones.

Figure 13 presents the radial profiles of the median and 16 (84) percentiles of (s, q, T) for DMO simulations inferred using EVIM, LSNUM, and LSIM. In contrast to the full hydrodynamical simulation, here the inferred s and q from EVIM and LSIM have radially progressively increasing profiles. Consequently, the radial profile of the triaxiality parameter decreases in both approaches though its actual value is larger in DMO than in the full hydrodynamical simulations. In Table 6, we present the median and 16 (84) percentiles of the shape and triaxiality parameters. Comparing this with Table 3, it is evident that s and q are reduced while T is increased (substantially) in DMO simulation (in EVIM).

Our results suggest that baryonic effects make DM halos more oblate. This result is in great agreement with the conclusion of Chua et al. (2019). In contrast, a DM halo looks more prolate for DMO in all of these approaches at small radii and gets more triaxial/oblate at larger radii. Furthermore, T is largest in EVIM and smallest in LSNUM.

In conclusion, baryonic effects play a crucial contribution in shaping the DM halo in MW-like galaxies.

5.2. Impact of FoF Group on Galaxy Morphology

So far we have only studied the impact of central halos in our analysis. Below we generalize our consideration and analyze the impact of different substructures, by using all particles associated with FoF groups in the shape of a DM halo. This means that we analyze all particles, including those belonging to the central galaxy as well as substructures in our computations.

First, we study the impact of including all FoF particles on the projected density diagram. In Figure 14 we display the logarithm of the projected x - y (number) density profile for the FoF group and a subsample of four galaxies of interest. As expected, there are many substructures in the FoF. It is

$\log_{10}(n/kpc^2)$ DMO Halo

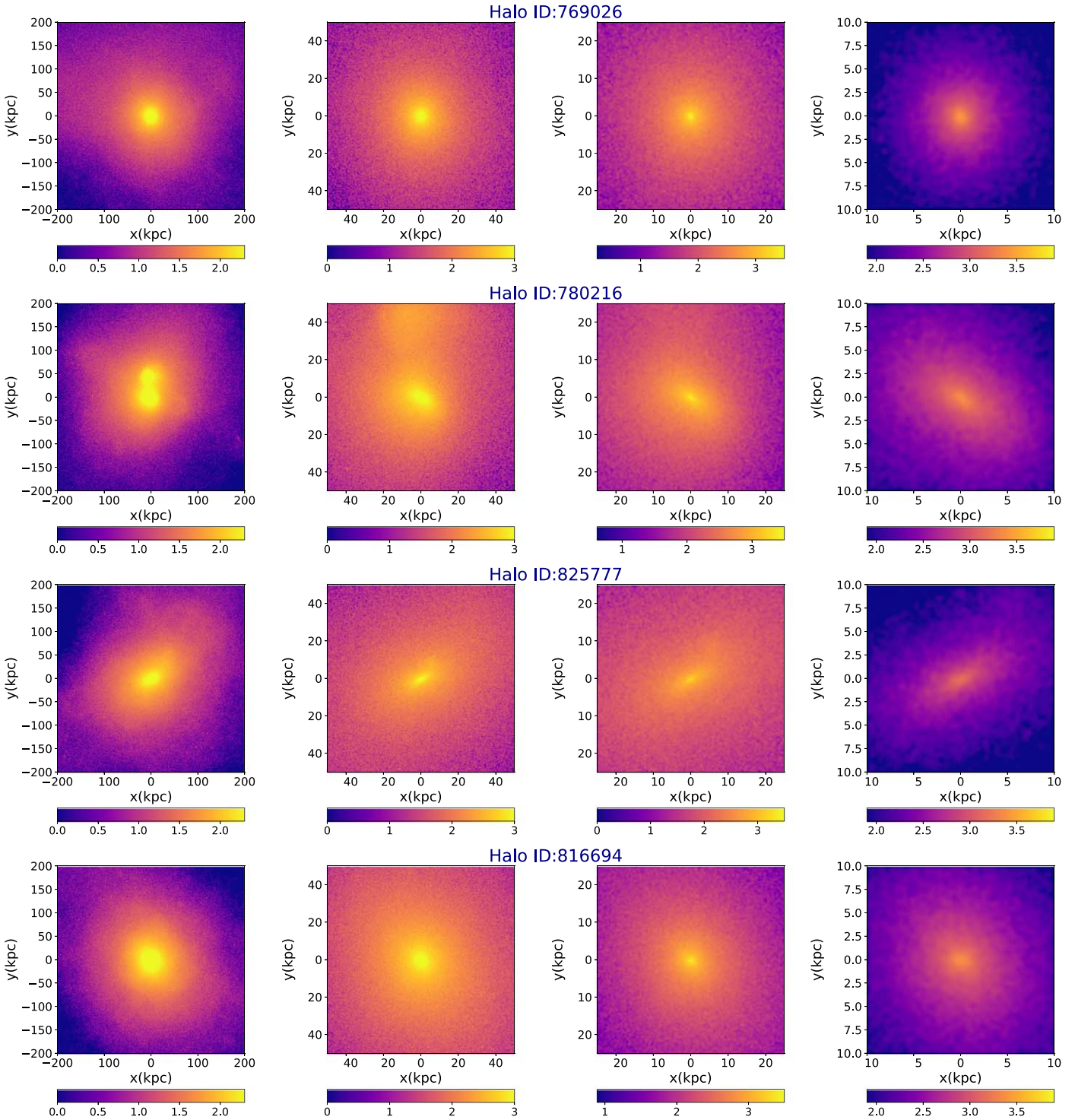


Figure 11. Logarithm of the projected number density of DM particles in the DMO run of MW-like galaxies. The halo ID is mentioned on the top of each row.

therefore intriguing how they could potentially affect the shape of the DM halo.

Having presented the central, DMO, and FoF group, it is intriguing to compare their shape profiles. To facilitate the comparison, in Figures 15 and 16 we present the axes/ r ratio and the shape parameters in all of the above three cases. To make the plots easier to read, we only show the results from our main algorithm, EVIM.

Figure 15 presents the axes/ r ratio for three MW-like galaxies in our galaxy sample. In each row, from left to right, we present this ratio for DM, FoF group, DMO, and DMO (FoF) simulations. A few points can be inferred from the figure. First of all, it is evident that, in the inner part of the halo, the impact of substructures is subdominant for both the hydro and DMO simulations. Next, the radial profiles of the axes/ r ratio are largely different between the full hydro and DMO

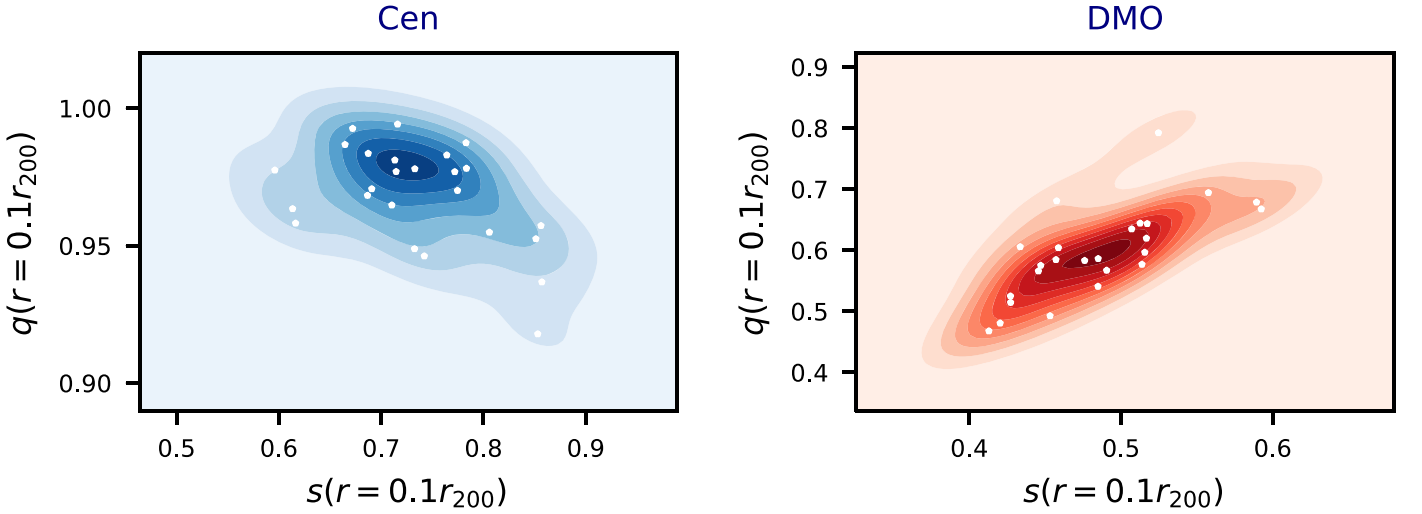


Figure 12. Correlation between s and q for different MW-like galaxies at $r = 0.1R_{200}$ for the central DM (left) and DMO (right) simulations. Overlaid on each plot is the scatter plot of s vs. q .

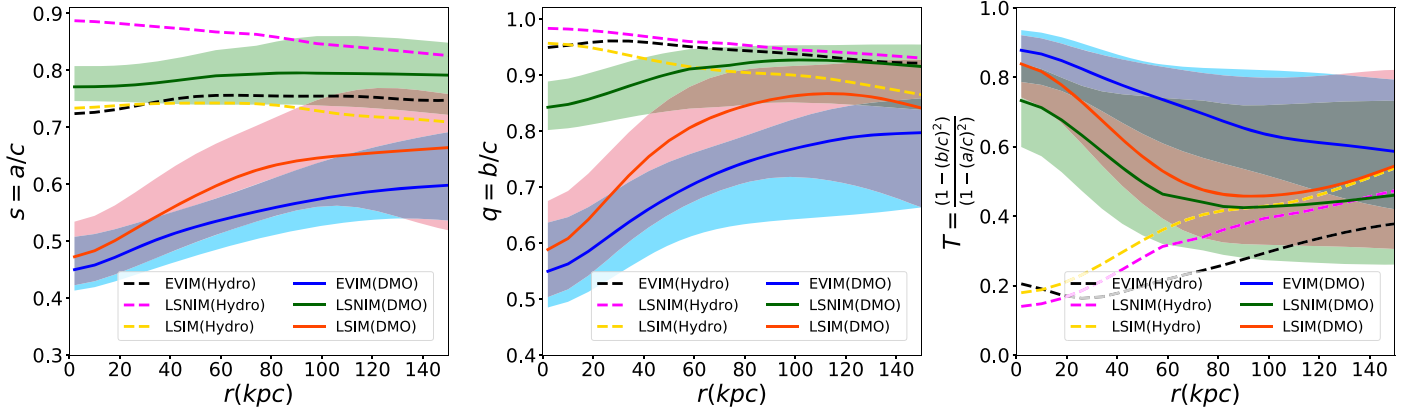


Figure 13. Comparison between the shape parameters s , q , and T for DM halos in DMO computed from EVIM, LSNUM, and LSIM. Overlaid on each plot is the median of the shape parameters from the hydrodynamical simulation (Hydro) as well.

Table 6

Median and 16 (84) Percentiles of DMO Shape Parameters Computed from EVIM, LSNUM, and LSIM

Method	s	q	T
EVIM	$0.571^{+0.063}_{-0.053}$	$0.764^{+0.052}_{-0.123}$	$0.635^{+0.188}_{-0.103}$
LSNUM	$0.789^{+0.042}_{-0.049}$	$0.912^{+0.034}_{-0.075}$	$0.488^{+0.249}_{-0.199}$
LSIM	$0.645^{+0.097}_{-0.130}$	$0.825^{+0.091}_{-0.164}$	$0.538^{+0.282}_{-0.221}$

simulations. This brings us to the picture that baryonic effects are more important in shaping the halos than the current substructures.

Figure 16 shows the radial profiles of the shape parameters s and q for three MW-like galaxies from our sample. Overlaid on every plot, we present the shape for DM, FoF group, DMO, and DMO(FoF) simulations. The shape profile of the FoF group is fairly close to the case of the DM halo in the inner part of the halo, up to 100 kpc. In contrast, the DMO simulation predicts a somewhat smaller value for the shape parameters.

5.3. Connection with Satellites

Having presented the Milky Way-like galaxies as central subhalos in every group, here we discuss the satellites in individual galaxies. Satellite galaxies are associated with the

subhalos, which are themselves members of their parent FoF halo. In IllustrisTNG simulations, subhalos are ordered in terms of their masses, with the heaviest member at the beginning of every group identified as the central galaxy, while the rest are assigned as satellites.

We adopt a stellar mass cut, hereafter M_* , in the mass range $M_* \geq 10^7 M_\odot$ to ensure that we study subhalos with more than ≈ 100 stellar particles, taking into account that the unit mass of baryons in TNG50 is $0.85 \times 10^5 M_\odot$. In addition, we restrict ourselves to distances less than 200 kpc. Furthermore, we also eliminate satellites that do not have a cosmological origin. In the TNG simulation, this is done by checking the ‘‘SubhaloFlag’’.

In Figure 17, we present the number of satellites within the above mass and distance ranges as a function of their median distance from the halo center. While more than the half of the satellites of simple and twisted halos are on average closer than 125 kpc, those associated with the stretched halo are mostly farther out. Furthermore, stretched halos have slightly fewer satellites than simple and twisted halos. Therefore, care must be taken when we draw a statistical conclusion about the current sample.

In Figures 18–20 we study the 2D distribution of the angle between the angular momentum of satellites and the closest eigenvectors associated with the minimum-to-maximum eigenvalues. Also, to compute and track the angle profiles, we

$\log_{10}(n/kpc^2)$ FOF DM Halo

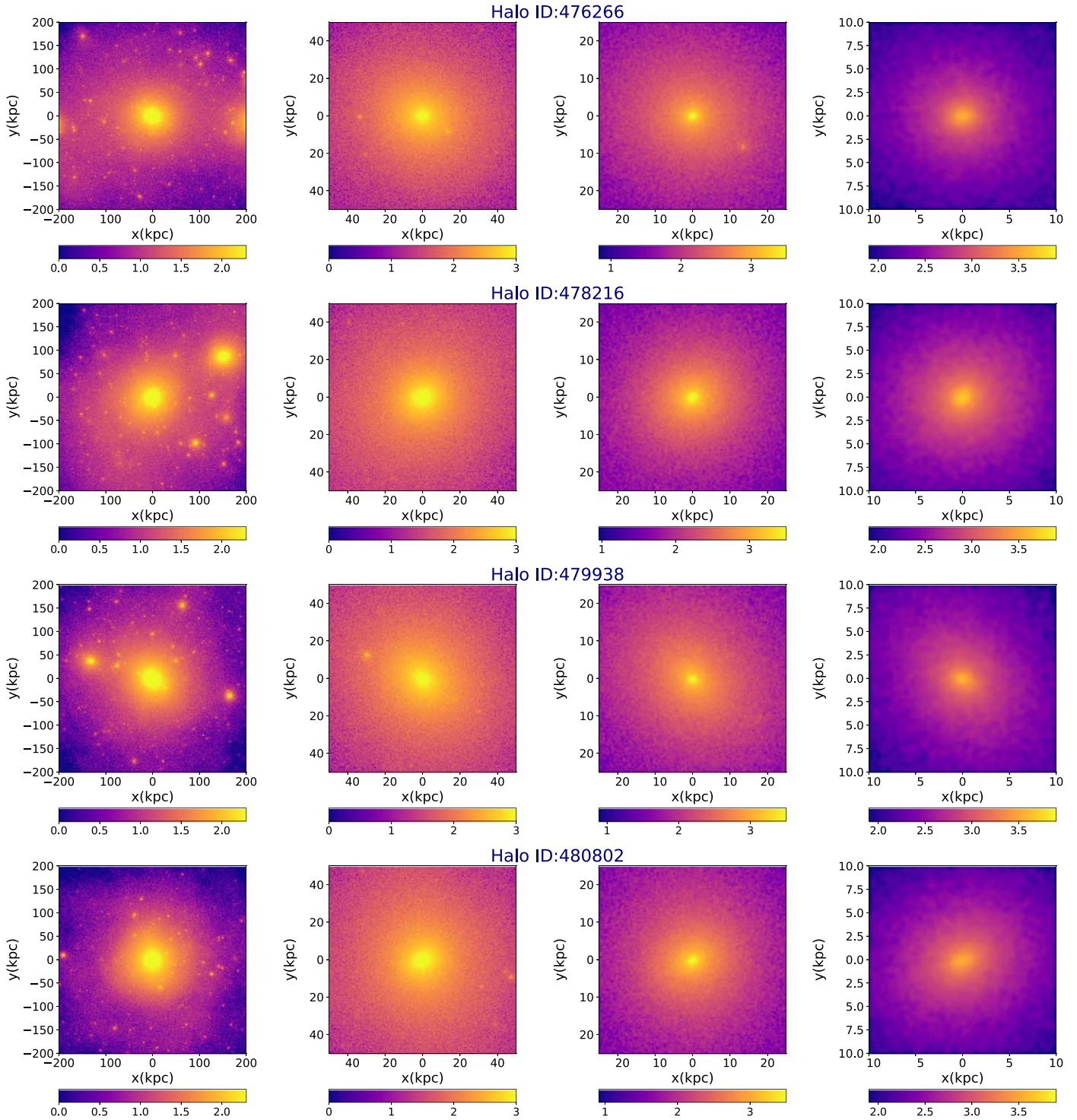


Figure 14. Logarithm of the projected number density of DM particles in the FoF group. The halo ID is reported on the top of each row.

propose that the angles are initially less than 90° . In each figure, from left to right, we draw the 2D distributions of all, simple, twisted, and stretched halos. There are few interesting points to learn from the above analysis.

1. The angular momentum of satellites is more aligned with the minimum eigenvector in simple halos than in the other two classes.

2. In twisted and stretched halos, there is a bimodality in the distribution of the angular momentum of satellites and the minimum eigenvectors computed at different locations. Almost half of satellites are antialigned (with angles around 180°) with the minimum eigenvector, while the others are in a similar range of angles to those associated with simple halos.

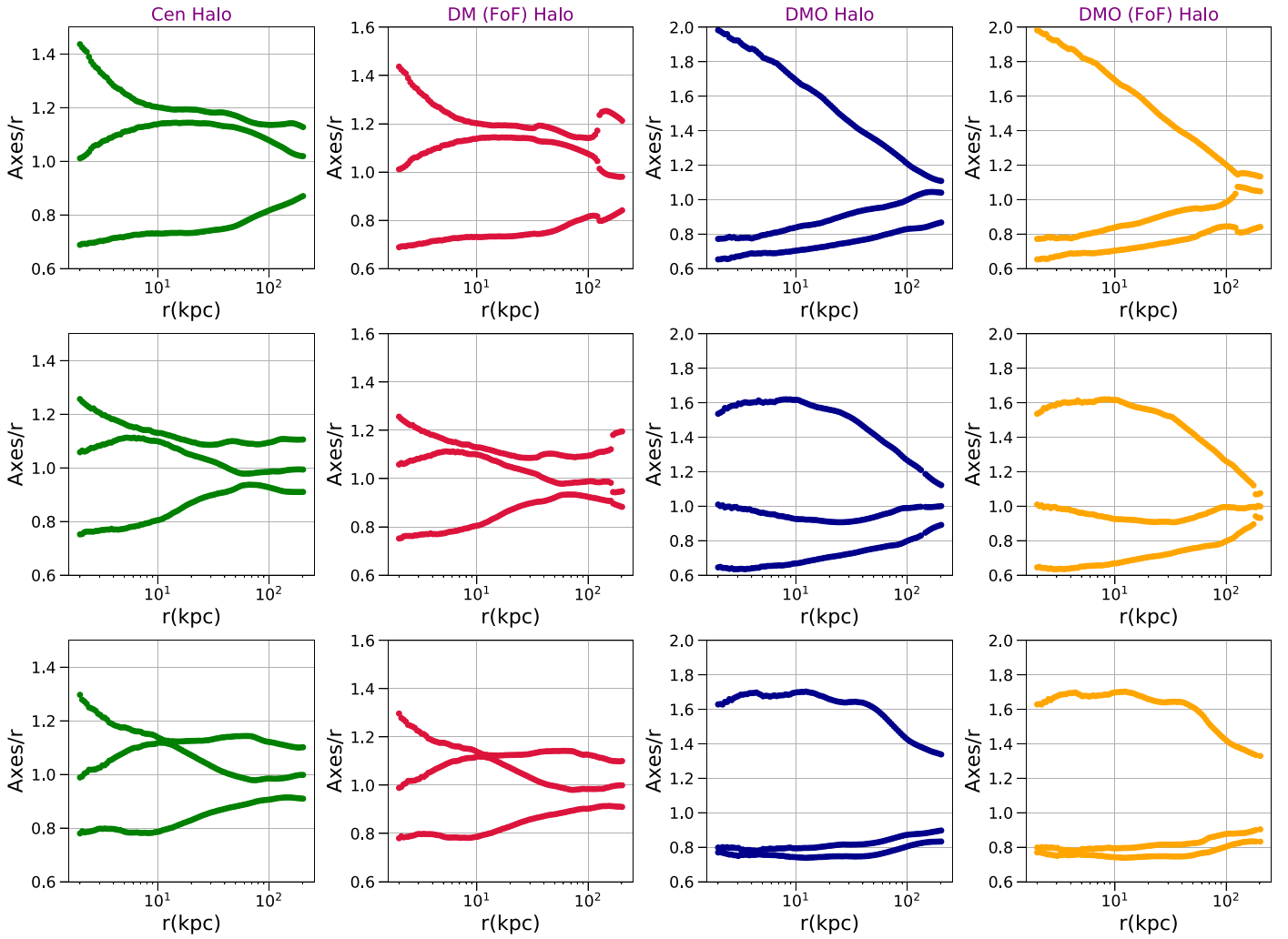


Figure 15. The ratio of axis lengths to the radius (r) for a subsample of MW-like galaxies in TNG50. From left to right, we present the axes/ r ratio for central DM (Cen), DM (FoF), DMO, and DMO(FoF) runs of TNG50. While the calculation including all FoF particles is fairly close to the case of the central halo only, DMO simulations look substantially different.

3. There is also a bimodality in the radial distribution of the satellites of simple and twisted halos. In particular, almost half of them are located closer than 100 kpc, while the rest are between 100 and 200 kpc.
4. While the angle profiles of the angular momentum of satellites and the minimum eigenvectors peak at around 40° , the radial profiles of the angular momentum of all satellites with intermediate and maximum eigenvectors peak at around 70° and 80° , respectively. This means that satellites are generally more aligned with the minimum eigenvector than with the intermediate and maximum ones.

Next, in Figure 21 we study the 2D distribution of the angle between the angular momentum of satellites and \mathbf{j}_{net} . From left to right, we present all, simple, twisted, and stretched halos.

From the plot, it is inferred that in the simple and twisted halos, θ_{SJ} mostly grows from left to right, where closer satellites are more aligned with \mathbf{j}_{net} than those farther out. There are, however, a few cases where simple/twisted halos are anti-aligned with \mathbf{j}_{net} . In contrast, in the stretched halos, θ_{SJ} seems to have a flat distribution.

Finally, in Figures 22 and 23, we present the 2D and 1D distributions of the infall redshift versus the radius and the infall redshift for satellites of different halo types. To infer the satellite's infall time, we trace each of them backward in time down to the redshift where the satellite no longer belongs to the central halo.

From Figure 22, it is inferred that, for simple and stretched halos, the infall time is mostly in the range $z = 0.3\text{--}1.0$ and less than 25% of satellites are accreted before $z > 1.0$. However, in twisted halos, there are some bimodalities in the distribution of the infall time of satellites, with about 39% of them being accreted at $z > 1.0$. Such bimodality is seen as the little bump in the 1D distribution of the satellite's infall time in Figure 23. Again we should note that since the current sample is limited, care should be taken in any statistical conclusions!

6. Connection to Observations

Thus far we have assessed the shape of the DM halo in MW-like galaxies in TNG50 using different techniques. Below we connect these theoretical outcomes to recent observational constraints on these shapes. Furthermore, since the radial distributions of shape parameters are rather different for

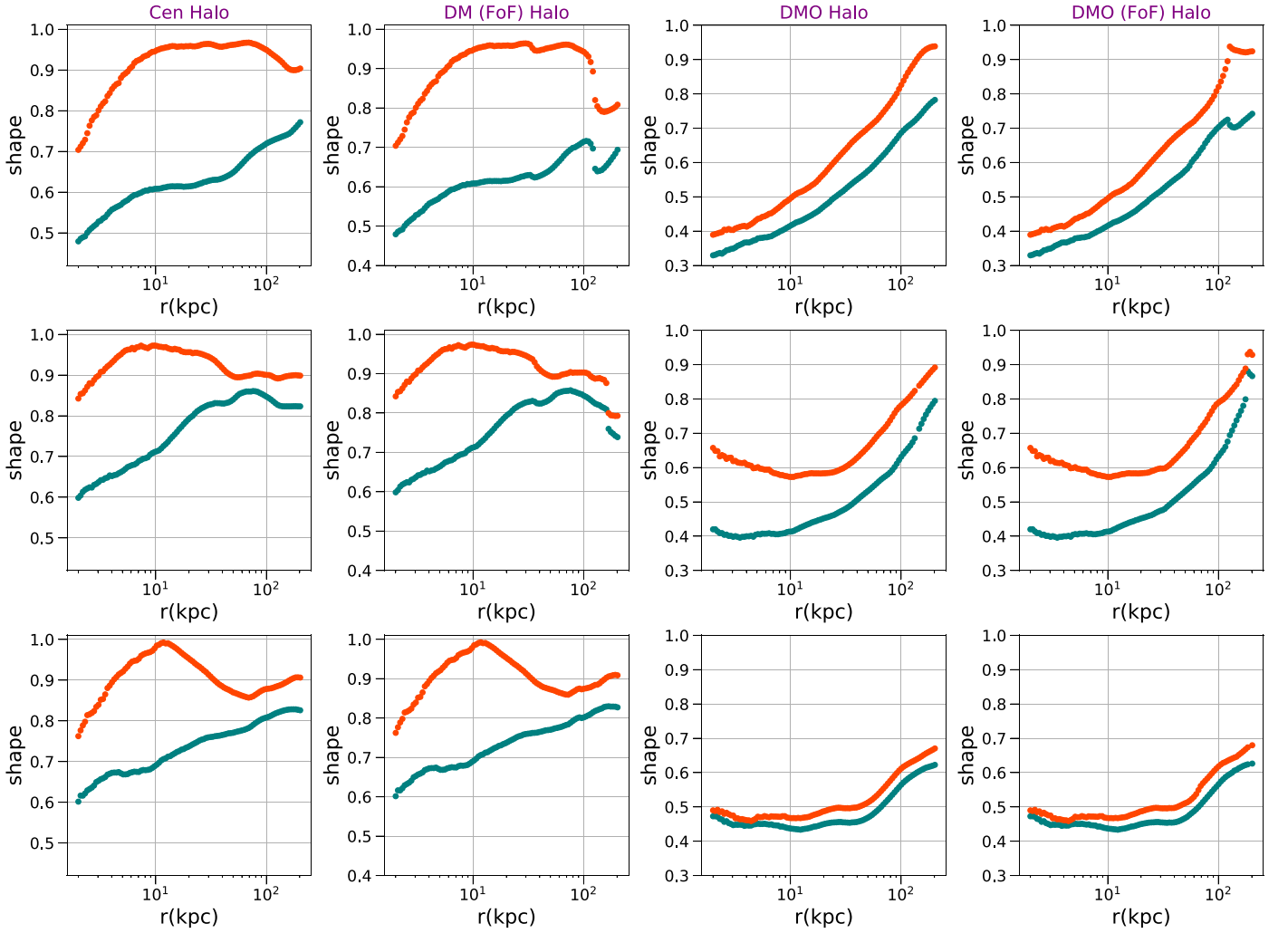


Figure 16. Radial profile of shape parameters for a subsample of MW-like galaxies in TNG50. From left to right, we present the radial profile of the shape in DM (Cen), FoF, DMO, and DMO(FoF) simulations.

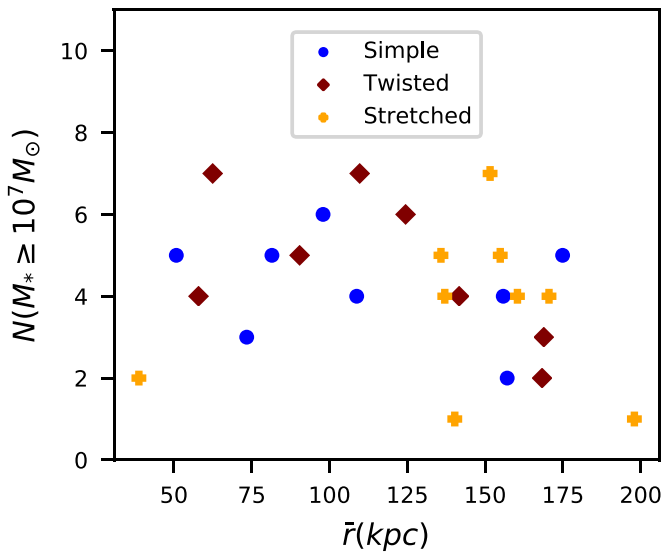


Figure 17. Number of satellites with stellar mass greater than $10^7 M_{\odot}$ (and at a distance less than 200 kpc) vs. the median distance of the satellites in this mass range from the center.

different techniques, we may be able to distinguish between them as well.

Observationally, one may indicate the shape of a DM halo without directly measuring this in the MW. Below, we use the observational constraints on the shape of DM halos as provided in Bland-Hawthorn & Gerhard (2016) and references therein.

One possible way to determine the DM halo shape in the MW is using the orbit of the Sgr dwarf across the sky. It was shown that the geometry of the stream across the sky confirms an oblate to near-spherical DM halo (Ibata et al. 2001; Johnston et al. 2005). More specifically, Johnston et al. (2005) used radial velocities of a sample of a few hundred M-giant candidates from the Two Micron All Sky Survey (2MASS) catalog to trace streams of tidal debris associated with the Sagittarius dwarf spheroidal galaxy (Sgr) that entirely encircle the MW. They strongly favored an isodensity $0.83 \leq s \leq 0.92$ at a distance of 13–60 kpc and ruled out $s \leq 0.7$ and $s \geq 1.1$ at 3σ . It is important to note that while both the shape parameters s and q for triaxial halos are by definition less than unity, in the context of axisymmetric halos, where the density profile is a function of $r^2 = x^2 + y^2 + z^2/q^2$, the flattening parameter s can be smaller/larger than unity for oblate/prolate halos.

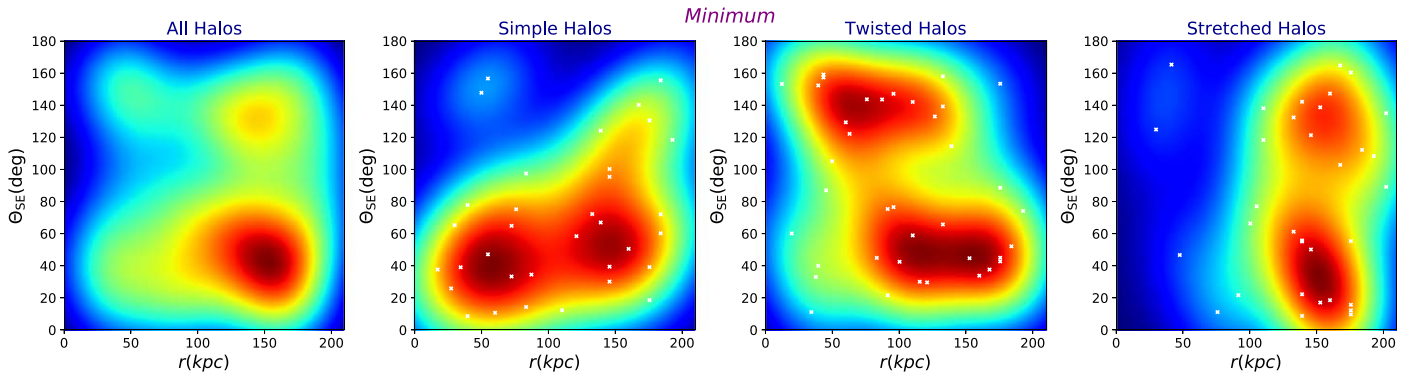


Figure 18. 2D distribution of the angle between the angular momentum of satellites and eigenvectors associated with the minimum eigenvalues of the inertia tensor located at the closest distance to individual satellites. Satellites of simple halos are in general more aligned with the minimum eigenvector. Twisted/stretched halos show a bimodal distribution of satellites. In each panel, marked crosses refer to individual satellites.

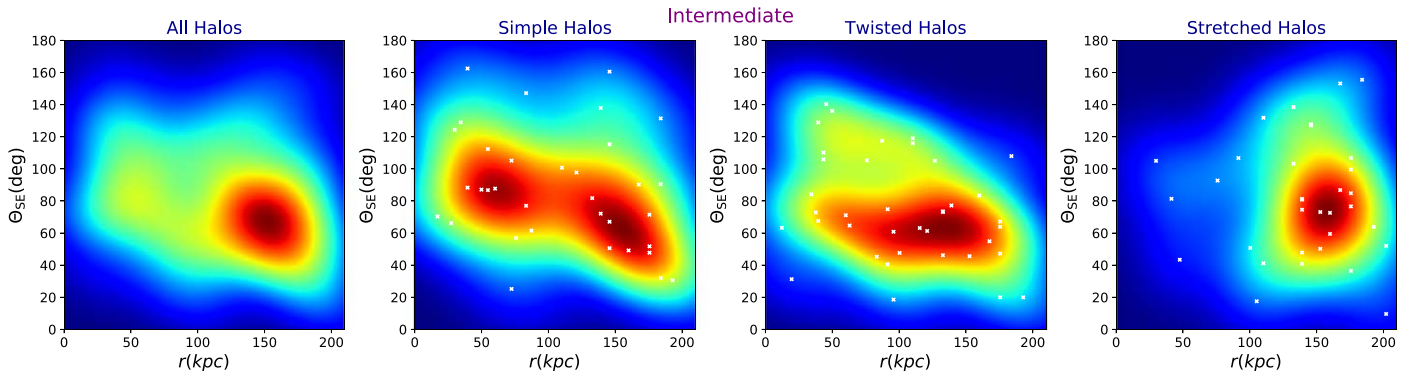


Figure 19. 2D distribution of the angle between the angular momentum of satellites and eigenvectors associated with the intermediate eigenvalues of the inertia tensor located at the closest distance to individual satellites. Satellites of simple halos are mostly orthogonal to the intermediate eigenvector. In each panel, marked crosses refer to individual satellites.

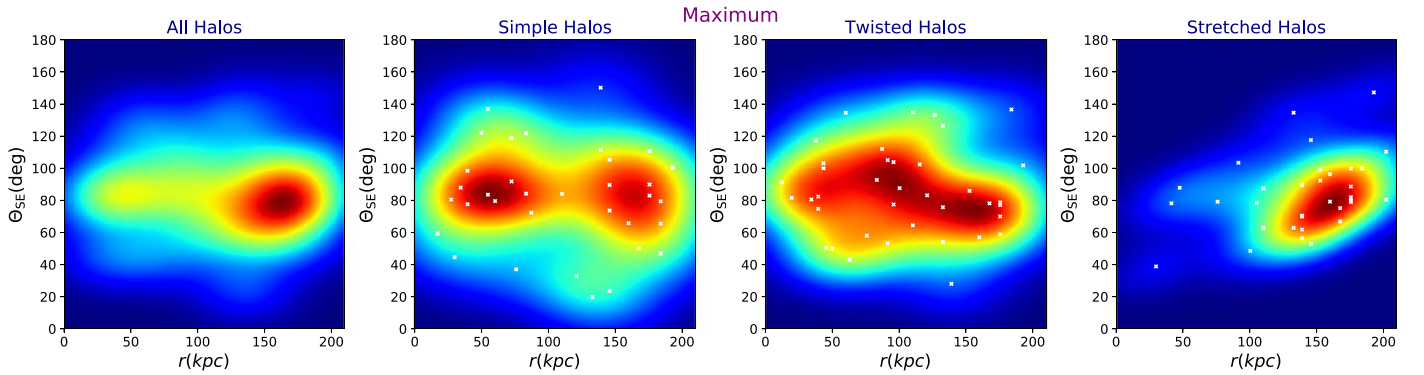


Figure 20. 2D distribution of the angle between the angular momentum of satellites and eigenvectors associated with the maximum eigenvalues of the inertia tensor located at the closest distance to individual satellites. Satellites of simple halos are almost orthogonal to the maximum eigenvector. In each panel, marked crosses refer to individual satellites.

Therefore, we make a transformation between the axisymmetric parameter (hereafter q_{axisym}) and our triaxial-based results. Below, we make the following transformation. If $q_{\text{axisym}} > 1$, we read $s = q = q_{\text{axisym}}$, and if $q_{\text{axisym}} < 1$, we shall take $s = q_{\text{axisym}}$ while $q = 1$.

Later, Helmi (2004) used line-of-sight velocities and compared the kinematics of the M-giant sample of Johnston et al. (2005) to the models of Sgr dwarf debris and showed that a portion of the mapped trailing stream is dynamically young and thus does not imply a strong constraint on the shape. On the other hand, the leading stream consists of older debris and

its dynamics provides a strong indication of a prolate halo shape with $s = 5/3$.

Kalberla et al. (2007) used data from the Leiden–Argentine–Bonn all-sky 21 cm line survey and derived the 3D HI density distribution for the MW to constrain the Galactic mass distribution. They found that a majority of DM particles can be modeled using an isothermal disk within $r \leq 40$ kpc. Though the confirmation of a DM disk is a hint of an oblate shape, they showed that a halo with a constant s does not quite match the observations and that the halo shape should be progressively prolate at larger distances.

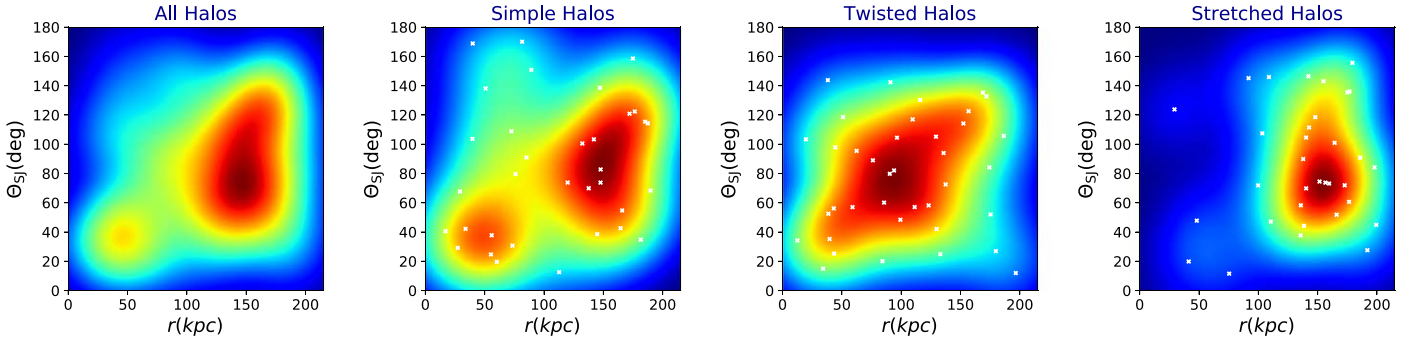


Figure 21. 2D distribution of the angle between the angular momentum of satellites and net specific angular momentum. In simple and twisted halos, θ_{SJ} grows with increasing radius, while in the stretched halos, θ_{SJ} has a flat distribution. In each panel, marked crosses refer to individual satellites.

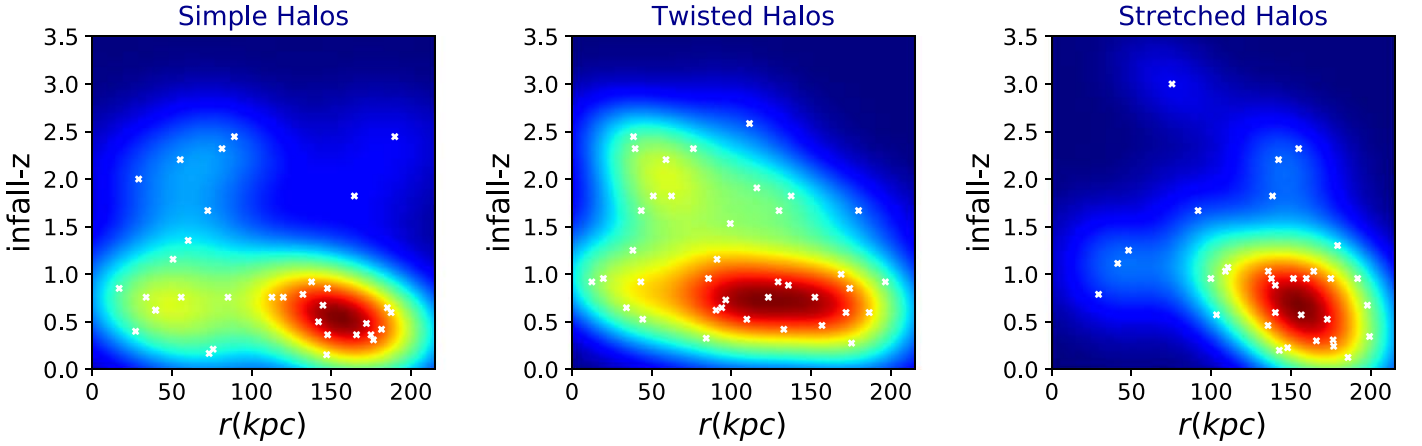


Figure 22. The 2D distribution of the infall time of satellites in different halo types in our sample. We have taken only satellites with masses above $10^7 M_\odot$ and at a distance of less than 200 kpc. In each panel, marked crosses refer to individual satellites.

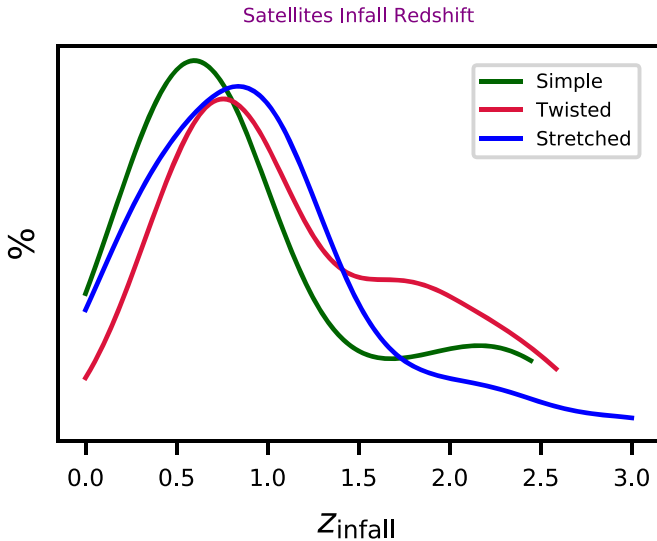


Figure 23. 1D distribution of the infall time for satellites in different halo types in our galaxy samples.

Koposov et al. (2010) combined Sloan Digital Sky Survey (SDSS) photometry, USNO-B astrometry, and SDSS/Calar Alto spectroscopy and constructed an empirical 6D phase-space map of the GD-1 stream of stars located at 15 kpc from the Galactic center, which is believed to be debris from a tidally disrupted star cluster. Using an axisymmetric potential, consisting of a stellar disk and DM halo, they found

$s_\Phi \geq 0.89$ at Galactocentric radii near to 15 kpc, where s_Φ refers to the flattening in the DM gravitational potential.

Garbari et al. (2012) used the kinematic and position data for ~ 2000 K-dwarf stars located near the Sun and at a distance of less than 1.1 kpc from the Galactic plane from Kuijken & Gilmore (1989) and determined the DM halo density in the MW. They reported a mild tension with the assumption of a spherical halo but consistency with an oblate DM halo with $s \geq 0.7$ or a local disk or a spherical DM halo with larger normalization.

Küpper et al. (2015) used the tidal streams from Pal5, the faintest and most extended globular cluster in the MW. They estimated the DM halo shape to be nearly spherical with a potential flattening $s_\Phi = 0.95^{+0.16}_{-0.12}$ at a heliocentric distance of 23.6 kpc. Using the proper motion of 75 globular clusters in Gaia DR2, Posti & Helmi (2019) estimated the mass and axis ratio of DM within $r \leq 20$ kpc. They reported a prolate DM halo with $q_{\text{axisym}} = 1.3 \pm 0.25$. This rules out a very oblate DM halo with $q_{\text{axisym}} < 0.8$ and a very prolate halo with $q_{\text{axisym}} > 1.9$ at 3σ .

Figure 24 summarizes the above constraints on the shape parameters of the DM halo. Overlaid on the plot are the medians of EVIM, LSNIM, and LSIM for both Cen and DMO simulations. We shall emphasize that all of the y-axes are located at $q=1$, the slight displacement is for clarity of presentation. Our results are comparable with most of these results. The level of agreement between the simulations and observational results is indeed excellent.

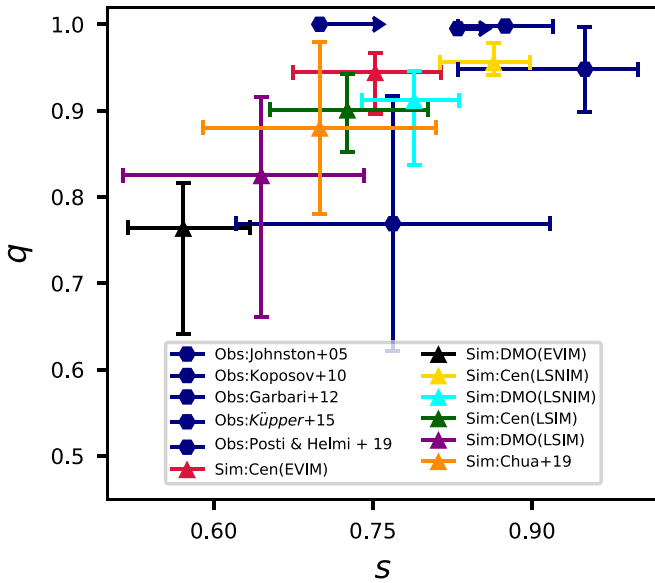


Figure 24. Different observational constraints on the shape parameters of the DM halo. Overlaid on the plot are the median of s and q for both the central (Cen) and DMO simulations analyzed by our three methods EVIM, LSNIM, and LSIM. Note with care that the results of Koposov et al. (2010) and Küpper et al. (2015) are based on the shape of the potential and not the shape of the DM distribution.

7. Summary and Conclusion

In this paper, we used the hydrodynamical simulation of TNG50 and extracted a sample of 25 MW-like galaxies identified using two different criteria. The first criterion is that the DM halo belongs to the mass range from $10^{12} M_{\odot}$ to $1.6 \times 10^{12} M_{\odot}$. The second is that Disk-frac, defined as the fraction of the number of stars with orbital circularity parameter $\varepsilon \geq 0.7$, is above 40%. We computed the radial profile of shape parameters (s , q) for a DM halo. We exploited three different approaches in our shape analysis. In the first approach, we inferred the halo shape using an enclosed volume iterative method, EVIM. In the second approach, we computed the shape using a local shell non-iterative method, LSNIM. Finally, in the third approach, we calculated the shape using a local shell iterative method, LSIM.

The radial profile of s is fairly similar between EVIM and LSIM in the inner part of the halo but slightly deviates beyond a radius of 80 kpc. In contrast, LSNIM predicts a larger profile for the s parameter, which progressively diminishes from the inner to the outer part of the halo. On the other hand, the radial profile of q is very close between EVIM and LSIM up to 10 kpc with a switchover behavior at larger radii, where EVIM gets closer to the LSNIM than LSIM.

Based on our shape analysis, which is mainly taken from EVIM, we classify DM halos in our galaxy sample into three main categories. Simple halos develop well separated eigenvalues that never cross each other (based on EVIM). But, owing to local fluctuations, they could pass through each other in LSIM. However, since our halo classification is based on the EVIM, we name this class simple halos. Furthermore, the eigenvector associated with the minimum eigenvalue in these halos is almost entirely parallel to \mathbf{j}_{net} . There are a total of eight halos in this class.

Twisted halos establish some level of gradual rotation throughout their radial profile. The level of reorientation varies

from one halo to another but in general the halo is reoriented in this radial profile. There are a total of eight halos in this class.

Stretched halos experience some levels of stretching (even in EVIM) in their radial profiles, where different eigenvalues cross each other. Consequently, the angle of their corresponding eigenvectors with different vectors varies by 90° at the location of stretching, thanks to the orthogonality of different eigenvectors. There are a total of nine different halos in this category.

We drew 3D ellipsoids for each category and established the rotation in the halo radial profile for each part.

We studied the main drivers of the DM halo shape. In this first study, we focused on three different drivers including the baryonic effects and the impact of substructures. For the first driver, we computed the halo shape in DMO simulations. We measured a smoother radial profile for (s , q) with a triaxial/prolate halo shape. This means that baryonic effects tend to decrease the diskyness of halos. Remarkably, in the DMO simulation, s and q increase with the radius. Accordingly, T decreases for both approaches. Our analysis showed that halos are simpler in DMO than in the full hydrodynamical simulation. This is suggestive and indicates that twisted/stretched halos may have some baryonic causes. Work is in progress to study these features in more detail.

We examined the effect of substructures in the shape in both the full hydro simulation and DMO simulations. Our analysis shows that in most cases the impact of substructures in the shape are subdominant in the inner part of the halo.

Furthermore, we also studied the location and angular momentum of MW satellites in the mass range $M_{*} \geq 10^7 M_{\odot}$ and at a distance of less than 200 kpc. We computed the radial profile of the angle between the angular momentum of satellites and min, inter, and max eigenvectors. Our analysis shows that the satellites of simple halos are more aligned with the minimum eigenvector than the other two classes. Furthermore, in twisted and stretched halos, instead, there is a bimodality in the distribution of the angular momentum of the satellites and the closest minimum eigenvector.

Furthermore, the distribution of the infall time of satellites shows that the majority of them are accreted onto the main halo between $z = 0.3$ and $z = 1.0$.

Finally, we connected our theoretical predictions for shape parameters to some recent observational studies. We overlaid our theoretical results on a few well studied tracers such as the stream of tidal debris, the GD-1 stream of stars, K-dwarf stars, and globular clusters from Gaia DR2 and found a fairly good agreement.

Since the radial profiles of the shape parameters are not the same, we may hope that more detailed observations at different radii will distinguish between different methods. For instance, it would be fascinating to use the spectroscopic data from Hectochelle in the Halo at High Resolution (H3) survey (Conroy et al. 2019) and compute the radial dependence of the shape for DM halos.

Throughout this work, we only studied the shape of the DM halo. In Emami et al. (2020), we generalize this study to the case of stellar halos and their possible connection to the DM shape as studied here.

It is a great pleasure to thank David Barnes, Angus Beane, Ana Bonaca, Dylan Nelson, Sandro Tacchella, Matthew Smith, and Annalisa Pillepich for very insightful conversations. We

especially acknowledge Charlie Conroy for his assistance with making the connection to observations. We thank the referee for their constructive comments that improved the quality of this paper. R.E. acknowledges the support by the Institute for Theory and Computation at the Center for Astrophysics. We thank the supercomputer facility at Harvard where most of the simulation work was done. M.V. acknowledges support through an MIT RSC award, a Kavli Research Investment Fund, NASA ATP grant NNX17AG29G, and NSF grants AST-1814053, AST-1814259, and AST-1909831. S.B. is supported by Harvard University through the ITC Fellowship. F.M. acknowledges support through the Program “Rita Levi Montalcini” of the Italian MIUR. The TNG50 simulation was realized with computer time granted by the Gauss Centre for Supercomputing (GCS) under GCS Large-Scale Projects GCS-DWAR on the GCS share of the supercomputer Hazel Hen at the High Performance Computing Center Stuttgart (HLRS).

Software: matplotlib (Hunter 2007), numpy (Van der Walt et al. 2011), scipy (Oliphant 2007), seaborn (Waskom et al. 2020), pandas (McKinney 2010), h5py (de Buyl et al. 2016).

Data Availability

Data directly related to this publication and its figures are available on request from the corresponding author. The

IllustrisTNG simulations themselves are publicly available and accessible at www.tng-project.org/data (Nelson et al. 2019), where the TNG50 simulation will also be made public in the future.

Appendix A Non-Disk Galaxies

As the main focus of this paper, so far we have merely studied the disk MW-like galaxies with more than 40% of stars in the disk, defined with $\varepsilon \geq 0.7$. From Figure 1 we inferred a very similar distribution for the orbital circularity parameter. In this appendix, we proceed further and study the distribution of the orbital circularity parameter for a subsample of galaxies with a smaller fraction of stars in the disk. In Figure 25 we present the distribution of ε for four galaxies with masses similar to the MW. At the top of each plot, we labeled Disk-frac. The plot considers four different Disk-fracs: 8%, 11%, 15%, 20%.

Unlike the case of disk MW-like galaxies with very similar distributions, here the distribution of ε varies a lot between different galaxies. It will be interesting to compute the shape for these non-disk galaxies. This analysis, however, is beyond the scope of this work and is left to a future study.

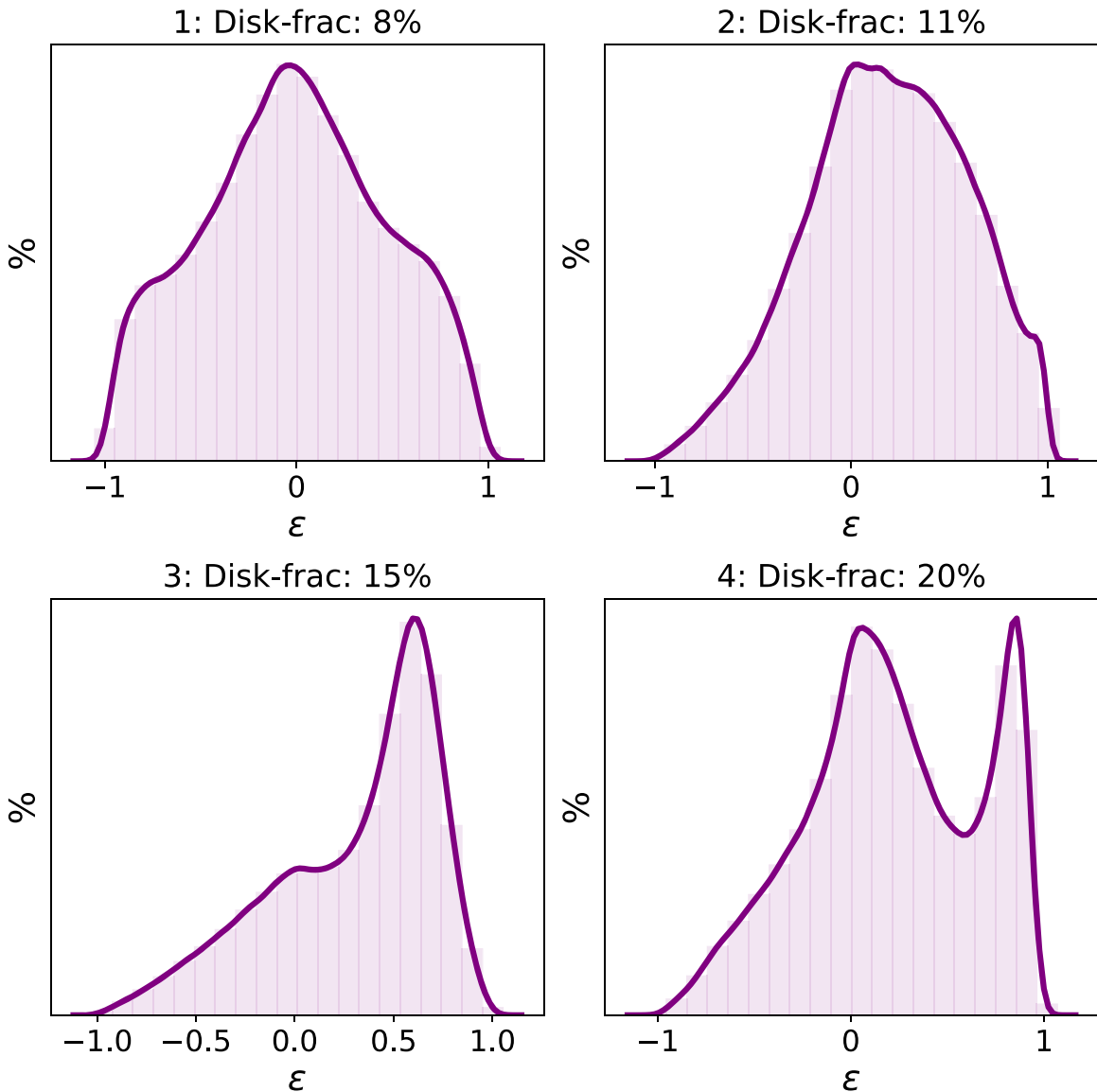


Figure 25. Distribution of orbital circularity parameter for a sample of four galaxies with masses similar to the MW. Disk-frac is indicated at the top of each plot.

Appendix B Convergence Check for Shape Analysis

As already mentioned in Section 3.1, our first shape finder algorithm, EVIM, relies on an iterative approach in which the algorithm is stopped after the shape parameters (s, q) converge such that $\max(T_s, T_q) \leq 10^{-3}$ where $T_s \equiv ((s - s_{\text{old}})/s)^2$ and $T_q \equiv ((q - q_{\text{old}})/q)^2$ refer to the residuals of the shape parameters (s, q) . Here we describe in more detail how the convergence is established in our approach. Furthermore, as a sanity check, we will also present a few examples with progressive reduction of the residuals from the above algorithm.

The convergence check in our shape finder algorithm proceeds as follows. First, we leave the system for at least 12 iterations before proposing any convergence criteria. This allows the system to become stabilized since its first couple of iterations are required to deviate from the initially proposed spherical symmetry. Then, to make sure that the convergence is truly established, we do not terminate the iteration once we get below the above threshold but allow the system to proceed and

wait until we have at least 15 consecutive cases with the residual below 10^{-3} . Since the spheroid is getting deformed at every iteration, it may well happen that the system experiences some sudden jumps and the residual increases from one iteration to the next. If that occurs, we will set the counter to zero and again seek 15 consecutive cases below the above threshold. This is a very reliable condition and in most cases reduces the residual substantially below 10^{-3} .

Appendix C Halo Classification

As already mentioned in the main text, we can identify different halo types based on our shape analysis: the so called simple, twisted, and stretched halos. Here we present the radial profile of the axes/ r ratio, the angle of min–inter–max eigenvectors with the unit vectors along the x, y, z directions of the simulation box, and the shape profile for all 25 halos in our galaxy sample.

Furthermore, in order to have unambiguous association of angles at the initial point and avoid the possibility of the

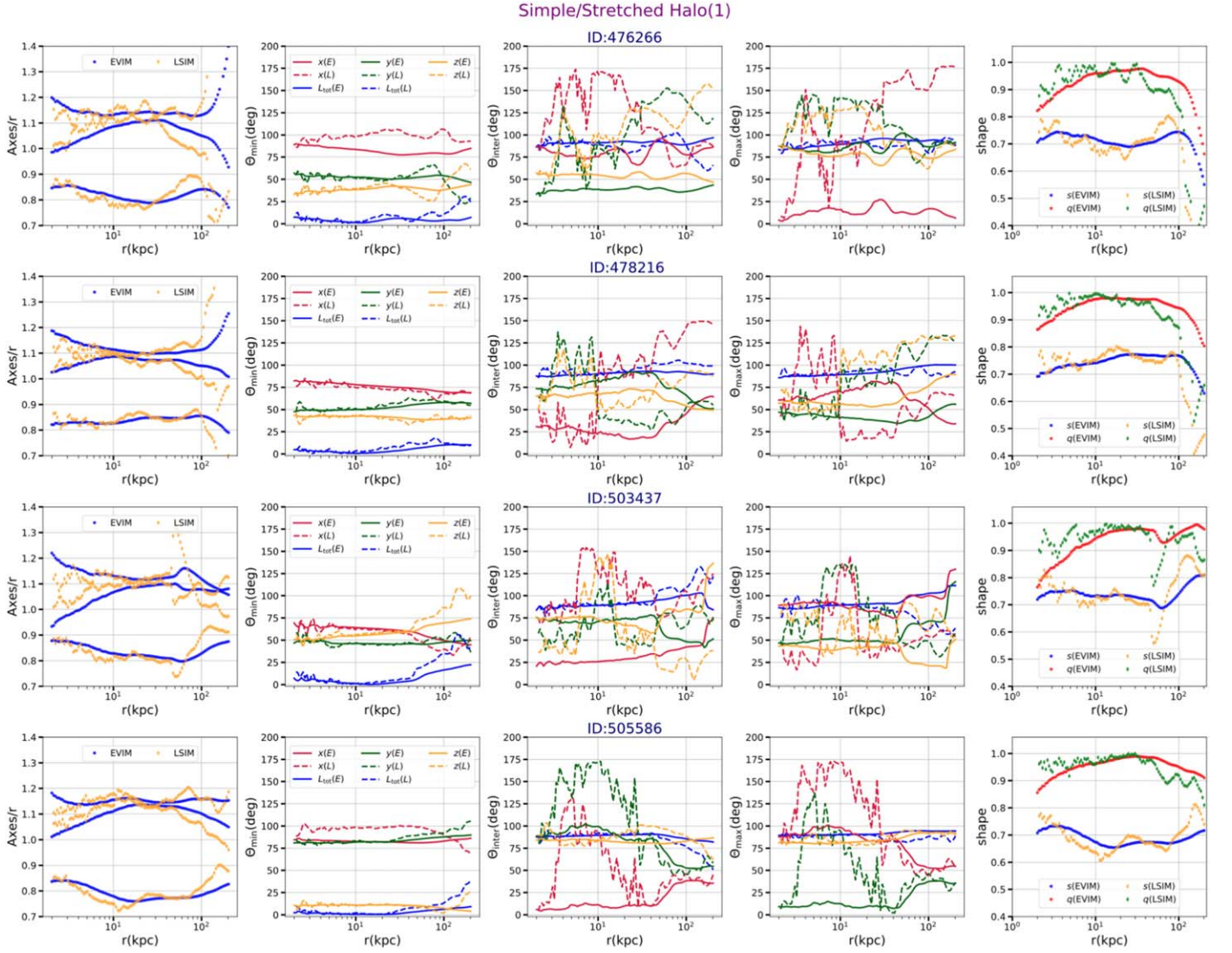


Figure 26. The radial profiles of axes/ r , angles, and shape parameters for the simple/stretched halos.

exchange of angles from very small to close to 180° , we propose that all of the angles are initially less than 90° . Depending on the halo type, some of these angles could grow and get bigger than 90° throughout their radial profiles. This is done by simply making a mask over the angle associated with the initial location and applying this to the entire radial profile of the angles.

C.1. Profile of Simple/Stretched Halos

We start with the simple halo class. In Figures 26 and 27, we present the radial profiles of axes/ r , angles, and shape parameters for this type. Overlaid on each figure, we also present the results from the LSIM method. Quite remarkably, the results of EVIM for axes/ r and shape parameters are fairly close to those of LSIM. However, since LSIM is sensitive to the local details of the shape, it is seen that there are some extra crossings of lines from LSIM, which lead to some extra rotations in LSIM. Because of this, in LSIM, we name this class simple/stretching. However, as we take EVIM as the main method, we call this group as simple halos to simplify the classification. The results of EVIM explicitly show that the

level of halo rotation is very minimal. There are a total of eight halos in this category.

C.2. Profile of Twisted Halos

Next, we study the twisted halos. In Figures 28 and 29, we analyze the radial profiles of axes/ r , angles, and shape parameters for this type. It is evident that halos in this category experience some gradual level of rotations from 50° to 100° in their radial profiles. There are a total of eight halos in this category. Overlaid on each figure, we also present the results from the LSIM. Interestingly, the outcomes of EVIM and LSIM are fairly close to each other.

C.3. Profile of Stretched Halos

Finally, we analyze the stretched halos. In Figures 30 and 31, we analyze the radial profiles of axes/ r , angles, and shape parameters for this type. Halos in this category experience one (or more) stretching where different eigenvalues cross each other. Consequently, the halos experience a change of angle of order 90° at the location of stretching. There are a total of nine halos in this class. Overlaid on each figure, we also present the

Simple/Stretched Halo(2)

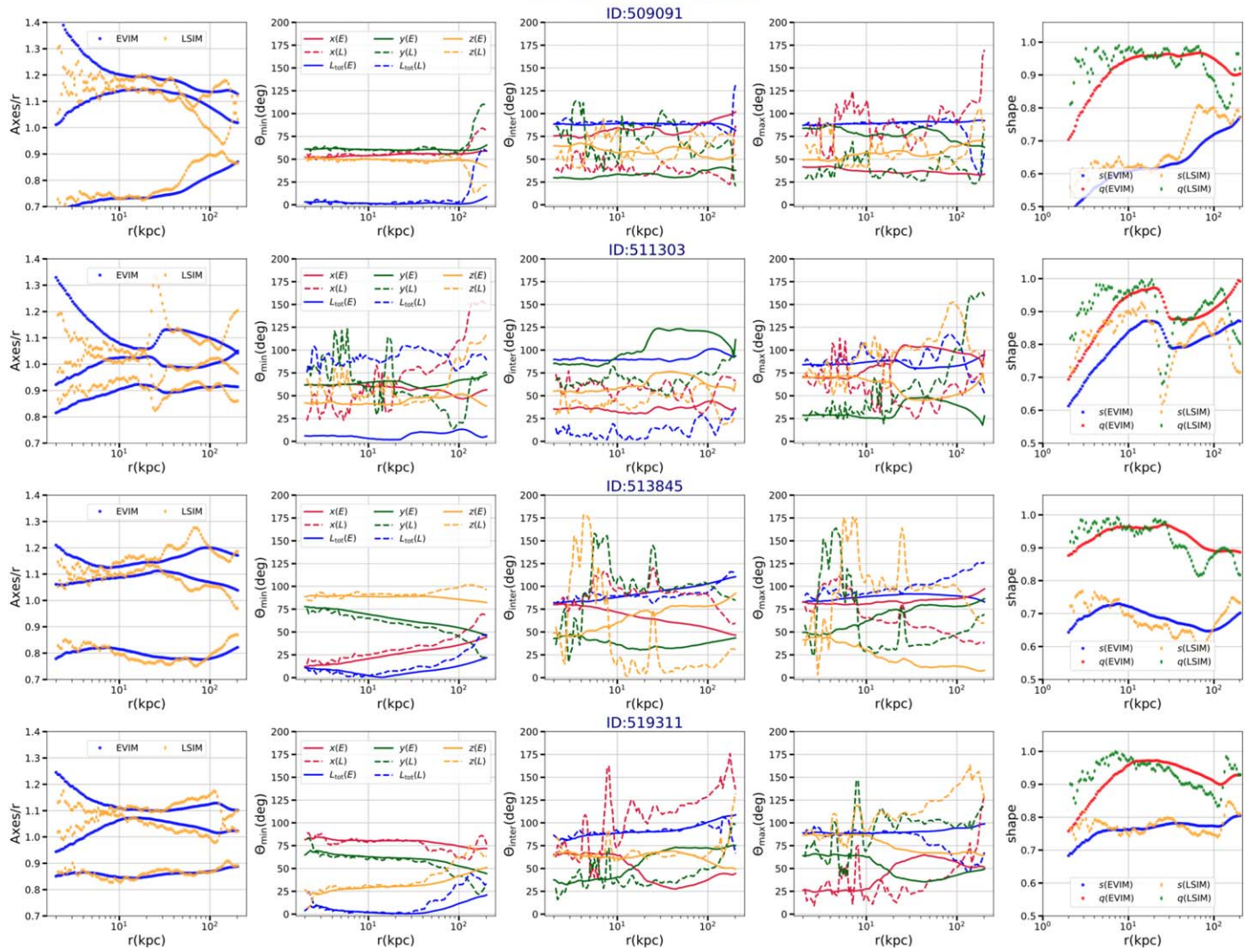


Figure 27. (Continued) The radial profiles of axes/ r , angles, and shape parameters for the simple/stretched halos.

Twisted Halo(1)

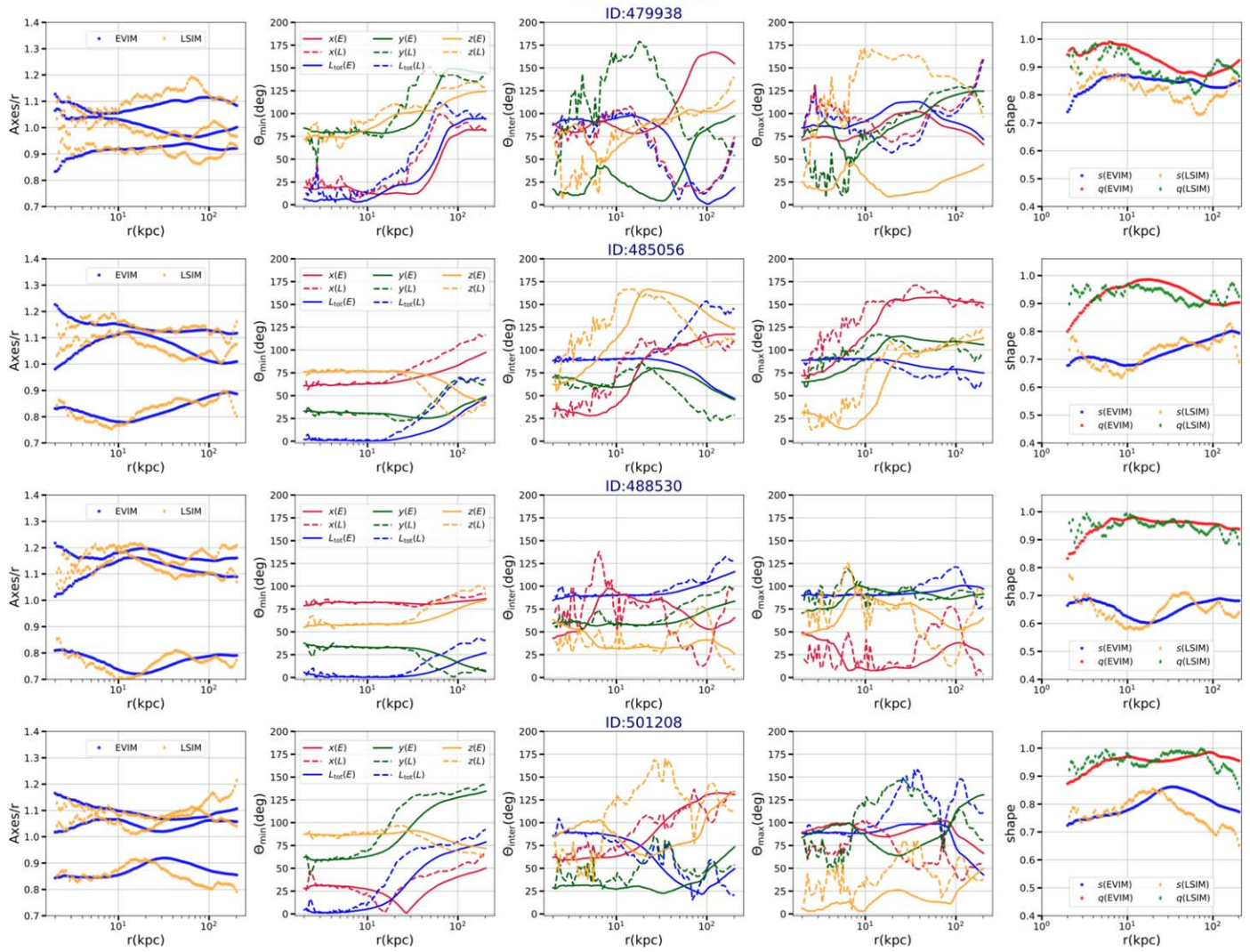


Figure 28. The radial profiles of axes/ r , angles, and shape parameters for the twisted halos.

Twisted Halo(2)

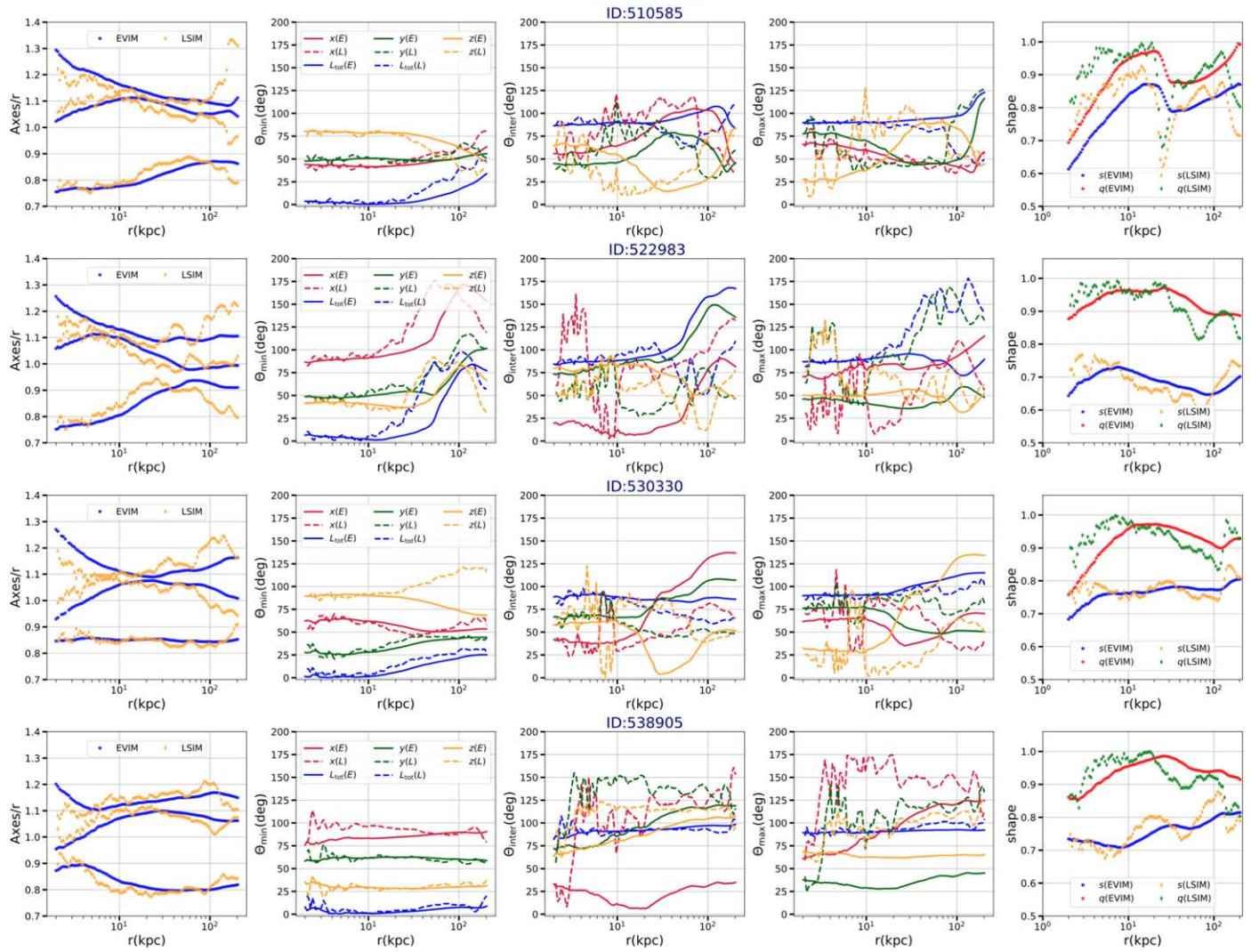


Figure 29. (Continued) The radial profiles of axes/ r , angles, and shape parameters for the twisted halos.

Stretched Halo(1)

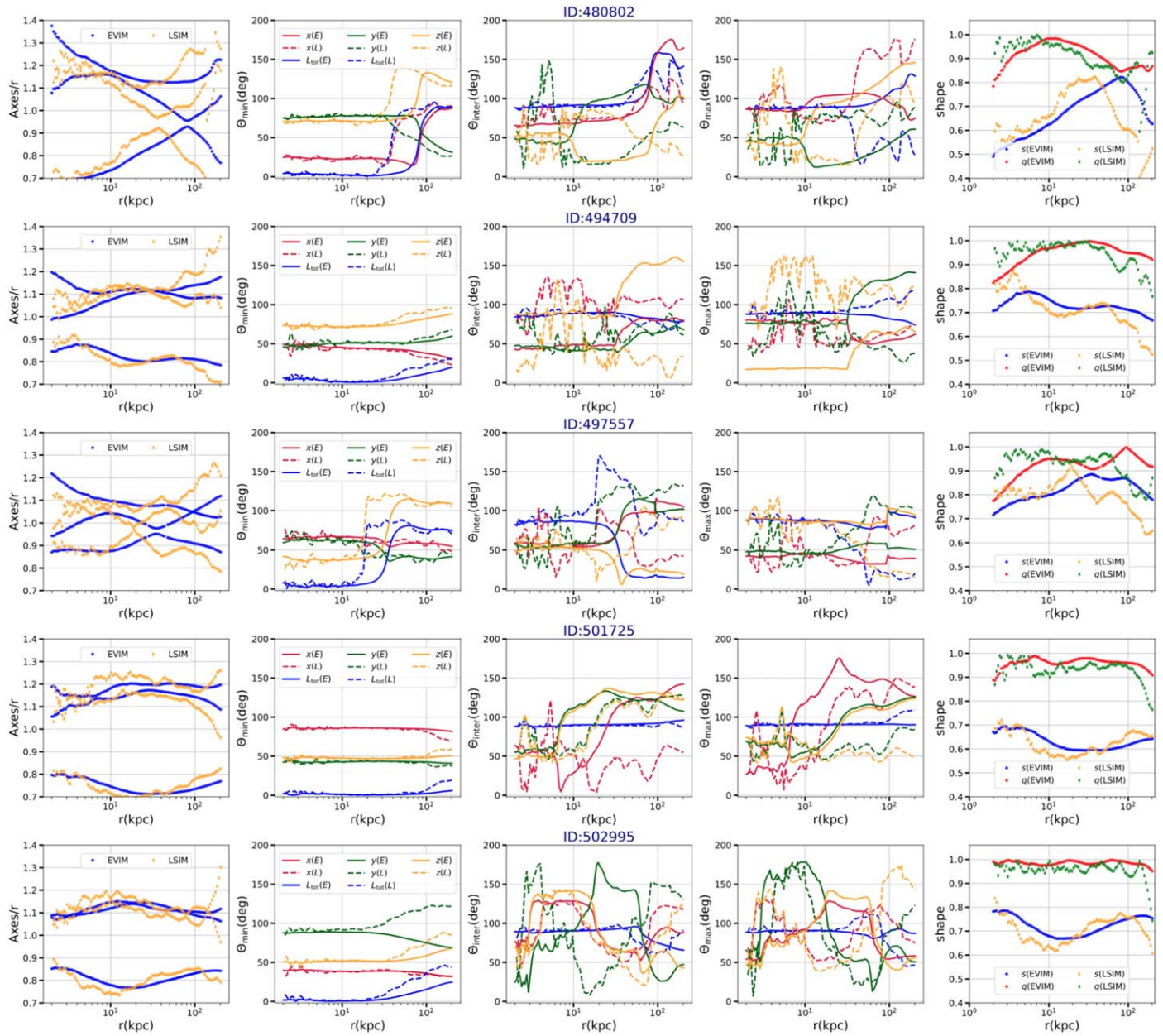


Figure 30. The radial profiles of axes/ r , angles, and shape parameters for the stretched halos.

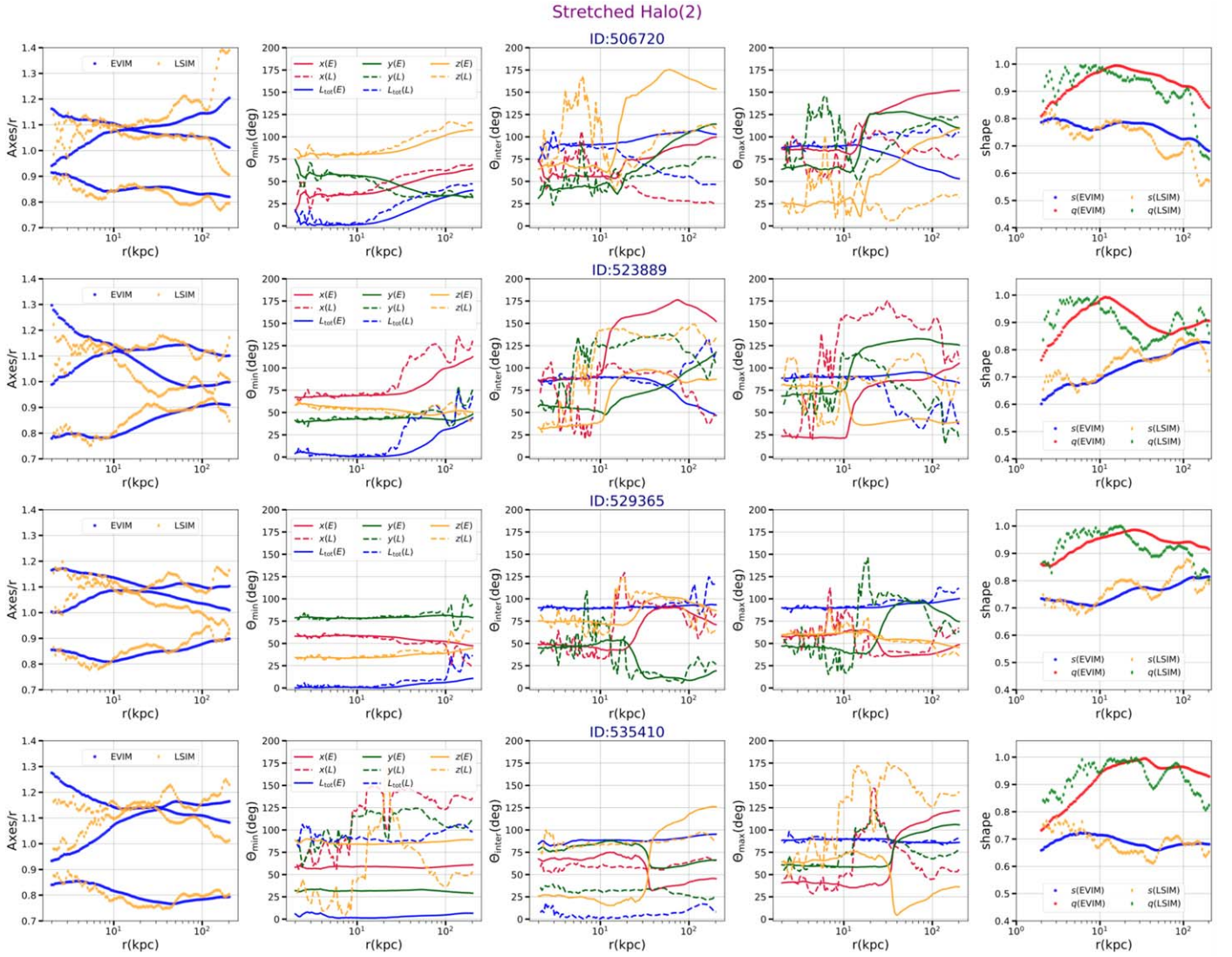


Figure 31. (Continued) The radial profiles of axes/ r , angles, and shape parameters for the stretched halos.

results from the LSIM. Interestingly, the outcomes of EVIM and LSIM are fairly close to each other.

Appendix D Impact of Weighting Factor on the Shape

We have presented different methods for analyzing the DM halo shape, and here we make a final comparison between them. Since

the inertia tensor depends on the weighting factor, here we check the impact of different choices on the final shape. In Figure 32, we examine the impact of $1/r^2$ and unity weighting factors in LSIM on the shape parameters. Overlaid on the figure, we also present the results from the EVIM. It is evident that the results of the LSIM from the above two choices of the weighting factors are almost the same. This is reasonable since we are dealing with very thin shells where the elliptical radii are almost one.

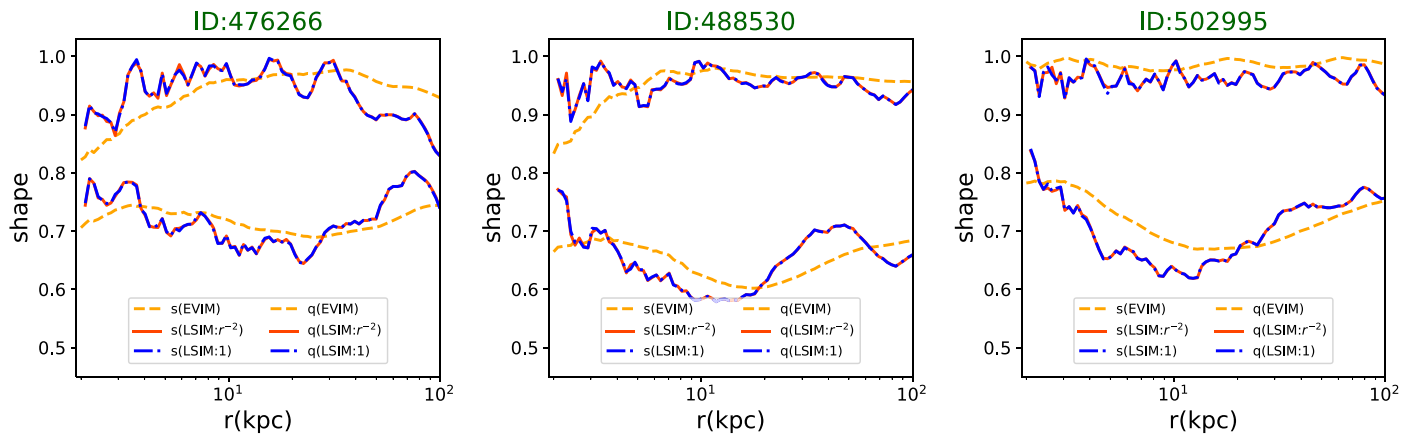




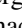





Figure 32. Impact of changing the weighting factor in shape parameters in a subsample of three MW-like galaxies.

ORCID iDs

Razieh Emami  <https://orcid.org/0000-0002-2791-5011>
 Shy Genel  <https://orcid.org/0000-0002-3185-1540>
 Lars Hernquist  <https://orcid.org/0000-0001-6950-1629>
 Sownak Bose  <https://orcid.org/0000-0002-0974-5266>
 Rainer Weinberger  <https://orcid.org/0000-0001-6260-9709>
 Federico Marinacci  <https://orcid.org/0000-0003-3816-7028>
 Abraham Loeb  <https://orcid.org/0000-0003-4330-287X>
 Paul Torrey  <https://orcid.org/0000-0002-5653-0786>

References

- Abadi, M. G., Navarro, J. F., Fardal, M., et al. 2010, *MNRAS*, 407, 435
 Abadi, M. G., Navarro, J. F., Steinmetz, M., et al. 2003, *ApJ*, 591, 499
 Allgood, B., Flores, R. A., Primack, J. R., et al. 2006, *MNRAS*, 367, 1781
 Bailin, J., & Steinmetz, M. 2005, *ApJ*, 627, 647
 Barnes, J., & Efstathiou, G. 1987, *ApJ*, 319, 575
 Bland-Hawthorn, J., & Gerhard, O. 2016, *ARA&A*, 54, 529
 Buck, T., Macciò, A., Ness, M., et al. 2018, IAU Symp. 334, Rediscovering Our Galaxy (Cambridge: Cambridge Univ. Press), 209
 Buck, T., Obreja, A., Macciò, A. V., et al. 2020, *MNRAS*, 491, 3461
 Butsky, I., Macciò, A. V., Dutton, A. A., et al. 2016, *MNRAS*, 462, 663
 Camps, P., & Baes, M. 2015, *A&C*, 9, 20
 Chua, K. T. E., Pillepich, A., Vogelsberger, M., et al. 2019, *MNRAS*, 484, 476
 Conroy, C., Bonaca, A., Cargile, P., et al. 2019, *ApJ*, 883, 107
 Crain, R. A., Schaye, J., Bower, R. G., et al. 2015, *MNRAS*, 450, 1937
 Davis, M., Efstathiou, G., Frenk, C. S., et al. 1985, *ApJ*, 292, 371
 de Buyl, P., Huang, M.-J., & Deprez, L. 2016, arXiv:1608.04904
 Dolag, K., Borgani, S., Murante, G., et al. 2009, *MNRAS*, 399, 497
 Dubinski, J. 1994, *ApJ*, 431, 617
 Dubinski, J., & Carlberg, R. G. 1991, *ApJ*, 378, 496
 Eisenstein, D. J., & Loeb, A. 1995, *ApJ*, 439, 520
 El-Badry, K., Quataert, E., Wetzell, A., et al. 2018, *MNRAS*, 473, 1930
 Emami, R., Hernquist, L., Alcock, C., et al. 2020, arXiv:2012.12284
 Font, A. S., McCarthy, I. G., Poole-Mckenzie, R., et al. 2020, *MNRAS*, 498, 1765
 Garbari, S., Liu, C., Read, J. I., et al. 2012, *MNRAS*, 425, 1445
 Garrison-Kimmel, S., Hopkins, P. F., Wetzell, A., et al. 2018, *MNRAS*, 481, 4133
 Genel, S., Vogelsberger, M., Springel, V., et al. 2014, *MNRAS*, 445, 175
 Gómez, F. A., White, S. D. M., Grand, R. J. J., et al. 2017, *MNRAS*, 465, 3446
 Grand, R. J. J., Helly, J., Fattahi, A., et al. 2018, *MNRAS*, 481, 1726
 Hani, M. H., Ellison, S. L., Sparre, M., et al. 2019, *MNRAS*, 488, 135
 Helmi, A. 2004, *ApJL*, 610, L97
 Hunter, J. D. 2007, *CSE*, 9, 90
 Ibata, R., Lewis, G. F., Irwin, M., et al. 2001, *ApJ*, 551, 294
 Jeon-Daniel, A., Dalla Vecchia, C., Haas, M. R., et al. 2011, *MNRAS*, 415, L69
 Jing, Y. P., & Suto, Y. 2002, *ApJ*, 574, 538
 Johnston, K. V., Law, D. R., & Majewski, S. R. 2005, *ApJ*, 619, 800
 Kalberla, P. M. W., Dedes, L., Kerp, J., et al. 2007, *A&A*, 469, 511
 Kazantzidis, S., Kravtsov, A. V., Zentner, A. R., et al. 2004, *ApJL*, 611, L73
 Kroupa, S. E., Rix, H.-W., & Hogg, D. W. 2010, *ApJ*, 712, 260
 Kuijken, K., & Gilmore, G. 1989, *MNRAS*, 239, 605
 Küpper, A. H. W., Balbinot, E., Bonaca, A., et al. 2015, *ApJ*, 803, 80
 Lambas, D. G., Maddox, S. J., & Loveday, J. 1992, *MNRAS*, 258, 404
 Law, D. R., & Majewski, S. R. 2010, *ApJ*, 714, 229
 Marinacci, F., Vogelsberger, M., Pakmor, R., et al. 2018, *MNRAS*, 480, 5113
 McKinney, W. 2010, in Proc. 9th Python in Science Conf., 445, 51
 Merritt, A., Pillepich, A., van Dokkum, P., et al. 2020, *MNRAS*, 495, 4570
 Monachesi, A., Gómez, F. A., Grand, R. J. J., et al. 2016, *MNRAS*, 459, L46
 Monachesi, A., Gómez, F. A., Grand, R. J. J., et al. 2019, *MNRAS*, 485, 2589
 Naiman, J. P., Pillepich, A., Springel, V., et al. 2018, *MNRAS*, 477, 1206
 Nelson, D., Pillepich, A., Springel, V., et al. 2018, *MNRAS*, 475, 624
 Nelson, D., Pillepich, A., Springel, V., et al. 2019, *MNRAS*, 490, 3234
 Nelson, D., Springel, V., Pillepich, A., et al. 2019, *ComAC*, 6, 2
 Oliphant, T. E. 2007, *CSE*, 9, 10
 Orr, M. E., Hayward, C. C., Medling, A. M., et al. 2020, *MNRAS*, 496, 1620
 Pandya, V., Primack, J., Behroozi, P., et al. 2019, *MNRAS*, 488, 5580
 Pillepich, A., Nelson, D., Hernquist, L., et al. 2018, *MNRAS*, 475, 648
 Pillepich, A., Nelson, D., Springel, V., et al. 2019, *MNRAS*, 490, 3196
 Pillepich, A., Springel, V., Nelson, D., et al. 2018, *MNRAS*, 473, 4077
 Planck Collaboration, Ade, P. A. R., Aghanim, N., et al. 2016, *A&A*, 594, A13
 Posti, L., & Helmi, A. 2019, *A&A*, 621, A56
 Prada, J., Forero-Romero, J. E., Grand, R. J. J., et al. 2019, *MNRAS*, 490, 4877
 Ravindranath, S., Giavalisco, M., Ferguson, H. C., et al. 2006, *ApJ*, 652, 963
 Rodriguez-Gomez, V., Snyder, G. F., Lotz, J. M., et al. 2019, *MNRAS*, 483, 4140
 Sandage, A., Freeman, K. C., & Stokes, N. R. 1970, *ApJ*, 160, 831
 Sanderson, R. E., Wetzel, A., Loebman, S., et al. 2020, *ApJS*, 246, 6
 Santistevan, I. B., Wetzel, A., El-Badry, K., et al. 2020, *MNRAS*, 497, 747
 Schaye, J., Crain, R. A., Bower, R. G., et al. 2015, *MNRAS*, 446, 521
 Schinnerer, E., Meidt, S. E., Pety, J., et al. 2013, *ApJ*, 779, 42
 Schneider, M. D., Frenk, C. S., & Cole, S. 2012, *JCAP*, 2012, 030
 Shao, S., Cautun, M., Deason, A. J., et al. 2020, *MNRAS*, in press
 Sijacki, D., Vogelsberger, M., Genel, S., et al. 2015, *MNRAS*, 452, 575
 Springel, V. 2010, *MNRAS*, 401, 791
 Springel, V., Pakmor, R., Pillepich, A., et al. 2018, *MNRAS*, 475, 676
 Springel, V., White, S. D. M., & Hernquist, L. 2004, in IAU Symp. 220, Dark Matter in Galaxies, ed. S. D. Ryder et al. (San Francisco, CA: ASP), 421
 Springel, V., White, S. D. M., Tormen, G., et al. 2001, *MNRAS*, 328, 726
 Tenny, A., Mandelbaum, R., Di Matteo, T., et al. 2015, *MNRAS*, 453, 469
 Thomas, P. A., Colberg, J. M., Couchman, H. M. P., et al. 1998, *MNRAS*, 296, 1061
 Trayford, J. W., Frenk, C. S., Theuns, T., et al. 2019, *MNRAS*, 483, 744
 Van der Walt, S., Colbert, S. C., & Varoquaux, G. 2011, *CSE*, 13, 22
 Van der Wel, A., Chang, Y.-Y., Bell, E. F., et al. 2014, *ApJL*, 792, L6
 Vogelsberger, M., Genel, S., Springel, V., et al. 2014a, *MNRAS*, 444, 1518
 Vogelsberger, M., Genel, S., Springel, V., et al. 2014b, *Natur*, 509, 177
 Vogelsberger, M., Marinacci, F., Torrey, P., et al. 2020, *NatRP*, 2, 42
 Warren, M. S., Quinn, P. J., Salmon, J. K., et al. 1992, *ApJ*, 399, 405
 Waskom, M., Botvinnik, O., Ostblom, J., et al. 2020, mwaskom/seaborn: v0.10.0 (January 2020), v0.10.0, Zenodo, doi:10.5281/zenodo.3629446
 Weinberger, R., Springel, V., Hernquist, L., et al. 2017, *MNRAS*, 465, 3291
 Zhang, H., Primack, J. R., Faber, S. M., et al. 2019, *MNRAS*, 484, 5170
 Zhu, Q., Marinacci, F., Maji, M., et al. 2016, *MNRAS*, 458, 1559